Parametric Waveform Synthesis: a scalable approach to generate sub-cycle optical transients

ROLAND E. MAINZ[1,2,†,*], GIULIO MARIA ROSSI[1,2,†], FABIAN SCHEIBA[1,2], MIGUEL A. SILVA-TOLEDO[1,2], YUDONG YANG[1,2], GIOVANNI CIRMI[1,2], AND FRANZ X. KÄRTNER[1,2]

[1]*Center for Free-Electron Laser Science CFEL, Deutsches Elektronen-Synchrotron DESY, Notkestr. 85, 22607 Hamburg, Germany*

[2]*Physics Department and The Hamburg Centre for Ultrafast Imaging, University of Hamburg, Luruper Chaussee 149, 22761 Hamburg, Germany*

† *These authors contributed equally*

[*]*roland.mainz@desy.de*

Abstract: The availability of electromagnetic pulses with controllable field waveform and extremely short duration, even below a single optical cycle, is imperative to fully harness strong-field processes and to gain insight into ultrafast light-driven mechanisms occurring in the attosecond time-domain. The recently demonstrated parametric waveform synthesis (PWS) introduces an energy-, power- and spectrum-scalable method to generate non-sinusoidal sub-cycle optical waveforms by coherently combining different phase-stable pulses attained via optical parametric amplifiers. Significant technological developments have been made to overcome the stability issues related to PWS and to obtain an effective and reliable waveform control system. Here we present the main ingredients enabling PWS technology. The design choices concerning the optical, mechanical and electronic setups are justified by analytical/numerical modeling and benchmarked by experimental observations. In its present incarnation, PWS technology enables the generation of field-controllable mJ-level few-femtosecond pulses spanning the visible to infrared range.

1. Introduction to parametric waveform synthesis

Over the past three decades, the development of ultrabroadband optical parametric amplifiers (OPAs) started a new era of ultrashort pulse generation [1–3]. Together with spectral broadening and compression techniques, OPAs allowed the generation of high-energy pulses with durations significantly shorter than the pump pulse they originate from. Originally developed with sub-ps duration pump lasers, the OPA has been adapted to longer pump pulses. In this case, it is often called optical parametric chirped-pulse amplification (OPCPA). Most of the analysis presented in this article applies to both OPA and OPCPA; in this case, we will refer to it as OP(CP)A.

Nonlinear broadening/compression techniques such as hollow-core fiber compressors [4] (HCFC), multi-plate continua [5] (MPC) or Herriott cells [6], allow broadening the spectrum of the initial pulse in an almost symmetrical way, therefore without strongly altering its central wavelength. These techniques are very efficient, but struggle to attain pulses that simultaneously span more than one octave of bandwidth, have high-energy and phase-stability. Therefore, standard broadening/compression techniques are not a scalable route for the generation of phase-stable high-energy pulses with durations below one optical cycle (sub-cycle), that requires more than one octave of bandwidth. Multi-octave spanning spectra supports non-sinusoidal waveforms, where the definition of an optical cycle becomes less precise as the pulse bandwidth increases. In general, when we refer to the pulse duration in terms of the number of optical cycles, the duration is defined by the intensity envelope full-width at half maximum (FWHM), whereas the optical cycle duration is related to the center-of-mass wavelength of the spectrum. Sub-cycle

non-sinusoidal IR waveforms are, for instance, applied in strong-field interactions such as high-harmonic generation (HHG), allowing for the generation of isolated attosecond pulses [7] and their tunability over the extreme ultraviolet/soft X-ray range [8].

Various OP(CP)As configurations have been demonstrated by using different nonlinear materials and optical configurations to cover the visible to mid-IR spectral region [1,3]. Moreover, OP(CP)A is a remarkably scalable technique that was demonstrated with attojoule [9] to joule [10] pulse energies and nW to kW average power [11]. Additionally, excellent carrier-envelope phase (CEP) stabilization can be achieved when OPA is carefully implemented. The CEP stabilization via OPAs is often better and more reliable than with broadening/compression sources that rely on active CEP-stabilization of the pump laser system. Exploiting difference-frequency generation (DFG) allows to create pulses with shot-to-shot stable CEP from pump pulses with fluctuating CEP [12]. Moreover, under particular conditions, the amplification of CEP-stable pulses via OPA does not add significant CEP-noise [13]. The coherent combination, also known as *synthesis*, of pulses generated by different sources, each covering a distinct spectral region, offers a way to achieve optical waveforms with multi-octave spanning spectra and durations below a single cycle. The coherent synthesis concept was early envisioned for CW-laser sources to redistribute the field intensity within the optical cycle and to create non-sinusoidal waveforms [14]. More recently, the synthesis of ultrabroadband pulses from OPAs has opened the way to create sculptured waveforms of high intensity and flexible bandwidth [15]. The synthesis of N pulses (with similar intensities) covering different spectral regions leads to a pulse whose intensity scales with N^2, since not only does the overall pulse energy increase by a factor N, but the temporal duration of the synthesized pulse shrinks by the same factor. The combination of multiple ultra-short pulses of different colors was first achieved by splitting the ultra-broadband output of a hollow-core fiber compressor and compressing different spectral regions individually [16]. This approach demonstrated the possibility of shaping complex electric field transients shorter than one optical cycle by controlling the CEP and the delay among the sub-pulses and allowed to achieve, for the first time, optical attosecond pulses. However, the limited spectral tunability and energy scalability of this approach motivated the development of OPA-based synthesizers [7, 17–22]. The high phase stability provided by OPA sources in combination with multi-octave spanning seed generation techniques such as white-light generation [23] (WLG) allows creating energy and bandwidth scalable sub-cycle waveforms via parallel synthesis [15] in a highly stable manner. The synthesized waveform can be shaped and stabilized in different ways, for instance, by controlling the relative delays (or the relative phases, RP) among the building pulses and their carrier-envelope phases (CEPs).

The increased versatility offered by OPA is achieved at the price of greater complexity than competing schemes. In order to achieve the coherent synthesis of multi-stage OP(CP)As, it is necessary to pay particular attention to the development of the optical and mechanical setup, as well as to implement an elaborate feedback control system.

In this paper, we describe the optomechanical setup and the control system implemented in our recently developed parametric waveform synthesizer [7]. In particular, we focus on different techniques that allowed to achieve exceptional waveform stability and waveform shaping while minimizing the control parameters and simplifying the overall control system. Analytical and numerical modeling of passive CEP-stabilization via DFG and of parametric amplification gave insight into which conditions maximize phase-stability and to develop an intuitive understanding of the different timing dynamics. This allowed us to simplify the waveform control system with respect to other approaches [17, 22] and to achieve stable and controllable pulse synthesis.

The paper is organized as follows: We start with an overview of the different laser technologies suitable to pump OP(CP)A synthesizers (Sec. 2). Afterwards we discuss the dispersion management and beam combination in parallel synthesizers (Sec. 3). It follows a discussion of phase stabilization, propagation and control (Sec. 4). In Sec. 5 we discuss the most important

aspects of the technical implementation. In Sec. 6 we describe the spatial properties of the synthesized beam and, in Sec. 7 we present results regarding the waveform stability and reproducibility. We conclude with the perspectives on the future development and applications of PWS (Sec. 8).

2. Pump laser technologies for OPAs

In this section, we will describe the main characteristics of laser sources suitable for pumping OP(CP)A-based waveform synthesizers, also called *parametric waveform synthesizers* (PWS). Broadband OP(CP)As can be pumped with a wide range of ultrafast laser sources. Over the last decade, several high-power ultrafast laser technologies have been developed. For instance, ytterbium-doped (Yb) laser systems based on Yb:Yttrium aluminum garnet (YAG) thin-disks [24], Yb-doped fibers [25], Yb:YAG slabs/rods [26, 27], Yb:YLF crystals [28] and Yb:KGW (Light Conversion) are viable options to pump parametric amplifiers with kW-level average powers. However, for several reasons, Ti:sapphire (Ti:Sa) amplifiers are still broadly used for OPA pumping. First, Ti:Sa amplifiers produce the shortest available pulse durations, down to 20-30 fs for mJ-level commercial systems. A pump pulse duration of ~ 100 fs is advantageous for OPA since it allows for stable white-light seed generation and simpler OPA output compression. The 800 nm central wavelength is also quite advantageous for pumping common nonlinear crystals such as beta barium borate (BBO) since both the fundamental and its second-harmonic (400 nm) allows for broad phase-matching bandwidth. The output power of commercially available Ti:Sa amplifiers is limited to ~ 15 Watt for room-temperature systems and to ~ 30 Watt for cryo-temperature ones. For many applications, Yb-based systems are usually the best choice if a high power is demanded. One particular advantage of the waveform synthesis scheme based on the parallel combination of OPAs is that it employs multiple pump beams, each pumping a different OPA. This allows to overcome the average power limitations of a single pump laser amplifier by using multiple parallel amplifiers.

Let us consider, for instance, a state-of-art Ti:Sa regenerative amplifier with 6 W average output power (typical for 1 kHz systems). As drafted in Fig. 1, by splitting and amplifying its output pulses by two consecutive double-crystal quasi-room-temperature (-10° C) single-pass amplifiers, it would be possible to obtain four beams with > 10 W each after compression (> 40 W of total power). The power of such a quasi-room-temperature four-beam Ti:Sa system could be even higher, on the order of 70-80 W, by operating at higher repetition rates (3-5 kHz) where common green pump lasers (frequency-doubled Nd:YLF/YAG) reach a higher power. While the

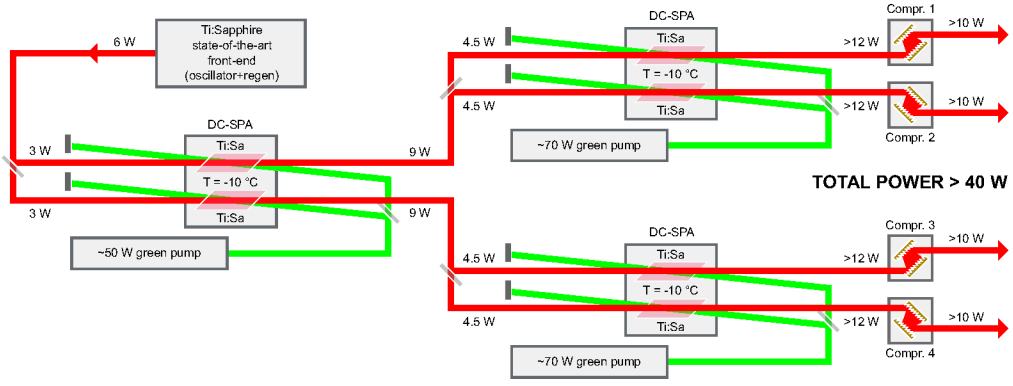

Fig. 1. Example of multi-beam laser system employing separate amplifiers for high-average power pumping of PWS. Scheme of a 4-beam quasi-room temperature Ti:Sa amplifier with > 40 W output power at 1 kHz in 4 tightly synchronized pulse trains.

multi-beam concept can be implemented with any laser technology, with Ti:Sa it is particularly advantageous since it is possible to have single-pass amplifiers with a gain of 2-3 and low B-integral. This allows to have just a few meters of non-common beam-path. Jointly with a small compressor size (compressed pulse energy $\leq$ 12 mJ), this is expected to result in a slight passive timing jitter among the output pulses, in the order of few-fs, while preserving an excellent beam quality. Such slight time jitter allows pumping different OPA stages with beams from different amplifiers without the need for active timing stabilization, as we will show in Sec. 4.5.

This possibility is also intriguing for Yb-doped amplifiers since the longer is the pump pulse duration the higher is the pump-seed jitter admissible in the OPCPAs. For instance, for 300 fs long pump pulses, an rms jitter up to 10 fs would be acceptable. This can be achieved by employing a common oscillator to seed the different amplifiers.

Regardless of the specific laser technology, one of the biggest challenges for PWS is the generation of a CEP-stable multi-octave spanning seed pulse. If the pump laser pulses are (sufficiently) CEP-stable, the seed pulse can be obtained directly by spectral broadening of the pump pulse. In case of non CEP-stable pump pulses, intra-pulse difference-frequency generation (DFG) or inter-pulse DFG can be implemented, as a first step, to realize CEP-stable pulses. Interpulse DFG, which allows for more freedom in choosing the seed central wavelength and for broader bandwidth, can be realized via white-light generation (WLG) and OPA (see Sec. 4). To produce a shot-to-shot phase-stable WL-filament the pump pulse must exhibit excellent beam quality and rms intensity fluctuations < 1%, due to intensity-phase couplings [29]. Moreover, in order to have a long-term stable WLG in YAG and Sapphire crystals a pump pulse duration between 100-300 fs (the shorter the better) is beneficial [30]. Since PWS usually requires several meters of beam propagation, pump beam pointing stability is also of paramount importance. Beam pointing can be actively stabilized, but since only slow drifts can be effectively compensated, the pump laser should not exhibit high-frequency beam-pointing fluctuations.

3. Ultrabroadband beam combination and dispersion management

The generation of ultrabroadband pulses with sub-cycle duration via PWS is enabled by cutting-edge multi-layered optical coatings. In fact, beam combination and dispersion management optics need to support multi-octave spanning spectra with high efficiency. The parallel synthesis scheme, with respect to the serial one, relaxes the constraints on dispersion management, since the dispersion can be managed individually in the different spectral channels, each having < 1 octave of bandwidth. Nevertheless, the dichroic mirrors used to combine the pulses must handle the full synthesized bandwidth. Moreover, it is convenient to use chirped mirrors supporting the full bandwidth to provide the final compression to avoid unwanted non-linearities during the beam transport into the vacuum beamline towards the experiment. The overall beam combination and dispersion scheme, comprising different dichroic mirrors (DMs), double-chirped mirrors (DCMs), and bulk materials, is shown in Fig. 2. For the realization of efficient multi-layered optics capable of dealing with the > 2-octaves of bandwidth, a new concept, named *dual-adiabatic-matching* (DAM) structure was developed [32]. The concept utilizes an additional double-chirp in the back section of the mirror to provide high transmission for long wavelengths. A comparison of the different chirped-mirror designs is shown in Fig. 3. Thanks to this advance, it was possible to design dichroic mirrors supporting > 2 octaves of bandwidth, capable of high reflectivity and controlled group delay for the short wavelengths and smooth and high transmissivity for the long wavelength, required for efficient splitting and combination of the overall PWS bandwidth. By cascading the dual-adiabatic matching structure in the front layers, as an ultrabroadband impedance matching section, it was possible to achieve >2-octave bandwidth double-chirped mirrors (DCMs), shown in Fig. 4. The average reflectivity of the ultrabroadband DCM pair is > 90%, and the calculated peak-to-peak values of the averaged residual group delay ripples are controlled to <5 fs over the whole bandwidth. The design of one of the dichroic mirrors and of

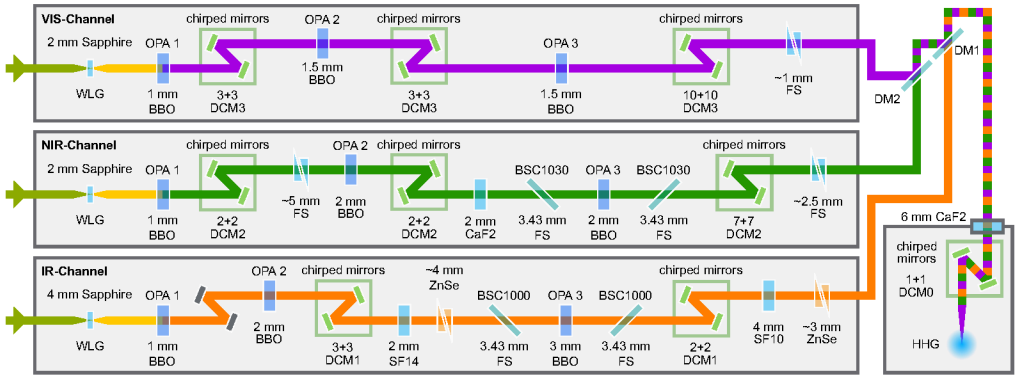

Fig. 2. Dispersion management scheme. The CEP-stable WLG driving beams are shown in light green color. The dispersion schemes for the infrared (IR, orange color) and near-infrared (NIR, green color) channels are completed, while the visible channel (VIS, violet color) it is still under development and its final dispersion scheme might slightly vary. Adapted from [31].

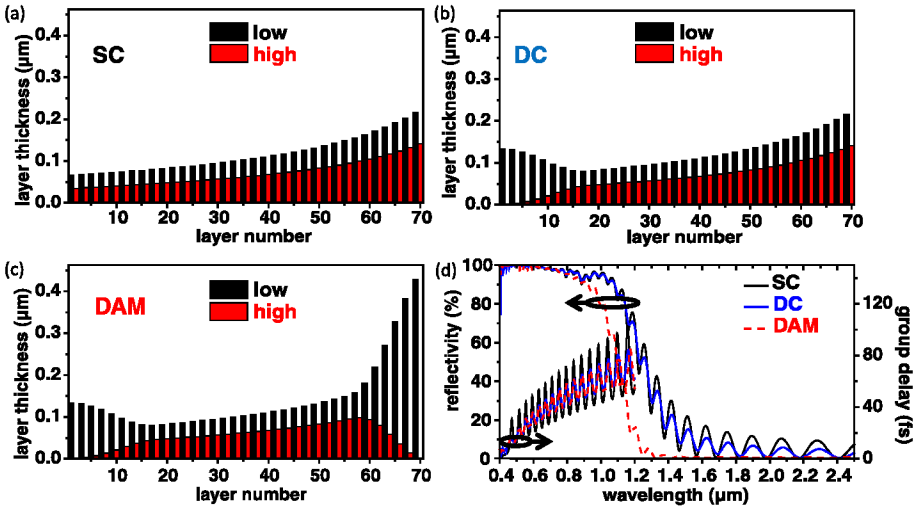

Fig. 3. Schematic of the multi-layer stack of (a) simple-chirped mirrors, (b) double-chirped mirrors, (c) dual-adiabatic-matching mirrors. (d) Reflectivity and group delay of the different mirror structures. Figure reproduced with permission from [32] ©The Optical Society.

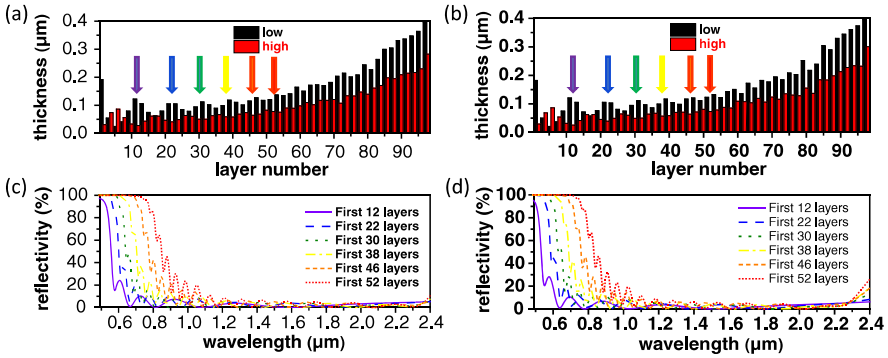

Fig. 4. **(a)** & **(b)** Schematics of the multi-layer stacks of the dual-adiabatic matching DCM pair, that provides negative dispersion over >2 octaves of bandwidth. **(c)** & **(d)** Reflectivity curves for different sections of the dual-adiabatic matching DCM structures in mirror (a) and (b), respectively. The colored arrows in (a) and (b) indicate to which depth in the multi-layer structure correspond the reflectivity curves of the same color. Each reflectivity curve exhibits an excellent anti-reflection behavior for the longer wavelengths. Figure reproduced with permission from [32] ©The Optical Society.

the final >2-octave spanning DCMs of the PWS are shown in Fig. 5 and 6 respectively. The

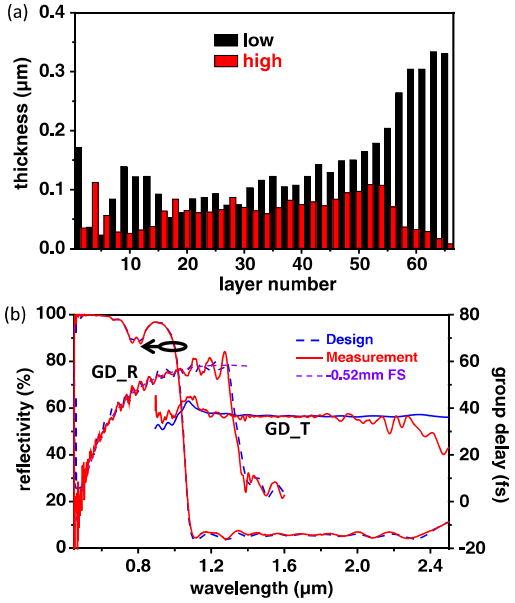

Fig. 5. **(a)** Structure of a dichroic mirror based on dual-adiabatic matching. **(b)** Designed and measured reflectivity and group delay of the dichroic mirror. The lower transmittance around 0.8 μm and the 5% reflectivity above 1.1 μm are intentionally realized to supply weak replicas of the incident pulses for timing synchronization. Figure reproduced with permission from [32] ©The Optical Society.

177
178 final dichroic mirrors feature a high contrast between the reflected and transmitted beam and an

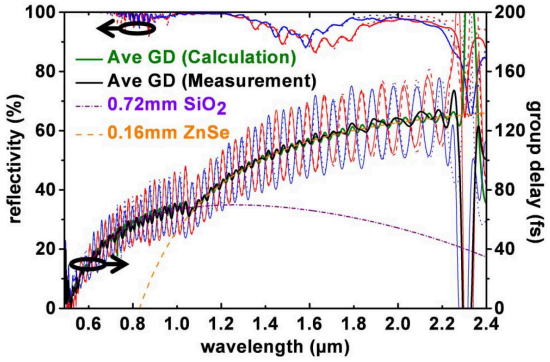

Fig. 6. Reflectivity and group delay of the ultrabroadband dual-adiabatic matched DCM pair. The dispersion of the DCM pair compensates a 1.44 mm propagation in fused silica for the wavelength in the 0.49–1.05 μm range, and compensates 0.32 mm propagation in zinc selenide for the wavelength in the 1.05–2.3 μm range. Figure reproduced with permission from [32] ©The Optical Society.

intentionally gradual spectral cross-over region, which allow us to obtain a few percent of energy of the two combined input beams at the secondary port of the beam-combiner. This weak replica of the main beam is used for the phase synchronization (see Sec. 4.7) and monitoring/stabilization of the spectra. Our current PWS setup will reach its full potential after the implementation of the third spectral channel in the visible range (VIS, 500-700 nm), which is already fully supported by our dispersion management scheme and beam combination optics. The overall supported bandwidth spans from 500 nm up to 2.2 μm. The parallel approach allows to scale this concept to even wider bandwidths. Extending further in the UV range is possible, although progressively difficult, due to a higher susceptibility of layer-deposition inaccuracies in the dielectric optics, which manifest stronger with shorter wavelengths. In the UV range, material-specific losses of the dielectric coatings must be avoided, which limits available material pairs. For further extension in the mid-IR these two challenges do not play a major role, and material combinations like Si:SiO_2 (> 2 μm) or Si:Al_2O_3 allow to extend the bandwidth up to ~ 7 μm [33]. The applied coatings can also exhibit non-linearities at high pulse intensities, and appropriate scaling of the mode size needs to be considered. Light to moderate nonlinearities can be included in the mirror design and precompensated. High-bandgap materials such as Nb_2O_5 might help further to manage nonlinearities [34].

Extending the PWS technology towards the mid-IR is also interesting for strong-field experiments such as HHG, to reach higher photon-energies [35].

4. Phase management in a parametric waveform synthesizer

In this section, we will analyze the fundamental mechanisms that are at the core of parallel parametric waveform synthesis (PWS). The dynamics that govern each nonlinear process used in a PWS, such as second-harmonic generation, white-light generation, and OP(CP)A have been the subject of numerous studies and are considered well-known. Nevertheless, since the PWS consists of dozens of nonlinear stages, many of which require synchronization between ultrashort pulses, it is helpful to develop a model in order to describe the impact of timing jitter on the phase of the pulses through the full PWS setup. This analysis has the objective of identifying the essential parameters for controlling the synthesis and clarifying the most critical noise sources by quantifying their impact on the stability of the final synthesized waveform.

We will initially focus on the longitudinal properties of the pulses since their stabilization

represents the biggest challenge in a parallel PWS. These properties are generically referred to as *temporal properties*. The transverse properties (or *spatial properties*) of the synthesis will be discussed in Sec. 6. Sec. 5 will present the most important aspects of the technical implementation of our PWS, in particular the timing and phase sensors and the low-latency feedback system to actively stabilize and control these longitudinal synthesis parameters.

Our PWS scheme (see Fig. 7) consists of several cascaded OPA-stages, and the pump-seed temporal synchronization is required at each stage. In particular, the temporal synchronization

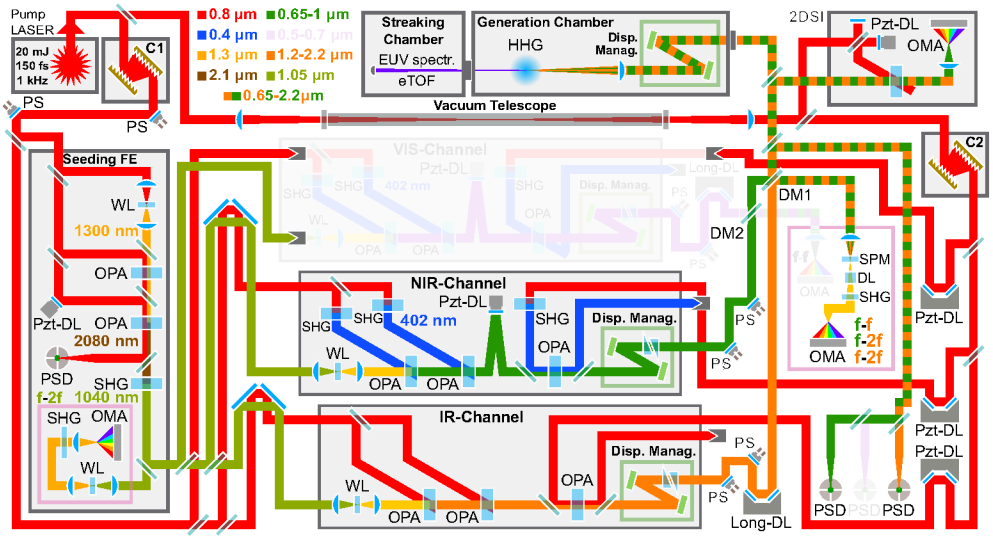

Fig. 7. Setup of a parallel PWS driven by a Ti:sapphire pump laser at 800 nm (1 kHz, 20 mJ). A fraction of the non-CEP-stabilized laser pulses drives the seeding front-end to derive a passively CEP-stable seed driver via DFG at 2 µm and its second harmonic at 1 µm. The second harmonic pulses drive separate WLG pulses in two parallel OPA-channels in the near-infrared (NIR) and infrared (IR) spectral range with three cascaded amplification stages each and partial recompression after amplification. A third planned spectral channel in the visible is shown in the shadowed area. A multi-phase meter at the final beam combination allows detecting all relevant phase-parameters. Long and short-range actuators within the system are used with a distributed feedback to stabilize the synthesis parameters. Adapted from [7].

among two different ultrashort pulses is required in 9 different components. The number will increase to 13 components once the visible channel is included. These components are the OP(CP)A stages and the dichroic mirrors at the synthesis points (DM1 and DM2 in Fig. 7), where the final OP(CP)A outputs are combined.

In this section, two questions will be answered: (i) What is the effect of timing jitter between pulses in these different components? (ii) How tight does the synchronization have to be in each component? We know that to achieve a stable waveform, the temporal synchronization required at the synthesis position is on the order of a fraction of the central wavelength, therefore in the hundreds of attoseconds domain. However, this strict timing requirement does not necessarily apply to all components mentioned above. We will demonstrate that it is required to achieve a tight synchronization in some OP(CP)A stages, while in other stages it is not necessary. This is particularly relevant since it would be extremely complicated to implement a large number of timing sensors, corresponding control actuators and feedback loops. Due to this limitation, it is strictly necessary to analyze the overall timing behavior of the system and find out which is

the minimum set of observables and corresponding actuators required to achieve a stable and controllable waveform synthesis.

In the following sections, we will start by analyzing the effects of pump-seed jitter in the OPA seeder, then consider the OPA amplifiers, and finally consider the synthesis process.

4.1. Phase-stable seed generation

In our PWS, we base the generation of an ultra-broadband and phase stable seed on the white-light generation (WLG) process [23]. With WLG, >2 octaves of seed bandwidth are readily available when driven with sub-ps pulses. The major drawback of this approach is that the seed pulse has only a pulse energy in the nJ-range, hence requires multiple OP(CP)A stages to reach the target energy of 0.1-1 mJ. On the other hand, WLG allows for multi-octave spanning spectra, tunable from the ultraviolet to the mid-IR range, exhibiting excellent coherence with respect to the driving laser pulse. In particular, the WLG of the PWS, which are driven by a passively CEP-stable pulse at 1040 nm in Sapphire crystals or YAG, can fully span across the 500-2500 nm region with low intensity fluctuations. Moreover, WLG exhibits excellent phase stability with respect to its driving pulse [29], which allows to maintain a high CEP-stability. The WLG, compared to higher pulse-energy seeding techniques like HCFC or MPC, seems to be favorable for PWS seeding since it allows to attain broader bandwidth and better shot-to-shot waveform stability. In our PWS, we implemented separate WLG-stages to prepare an optimized seed for each spectral channel. Earlier observations hinted to a sufficient phase-stability for such a separate WLG/OPA system [36]. With such an approach, one can adapt to the requirements of each spectral channel by the choice of the nonlinear material, its thickness, focusing conditions and pumping intensity. To experimentally verify that such a parallel seeding approach is feasible, we characterized the WL phase stability by realizing a Michelson interferometer with two separate WLG stages, one in each arm. Two replicas of 800 nm pulses drive the WLG stages as shown in Fig. 8 (a). When both WLG outputs are superimposed, a spectral interference will be observed, and a single-shot every-shot spectrometer quantifies the relative phase-noise among the WLGs. The environmental distortions of the interferometer, such as thermal drifts and air convection, were removed by a low-bandwidth feedback acting on a piezo-actuated delay-line (Pzt-DL) in one of the interferometer arms (Fig. 8 (a)).

A residual phase noise of 32-65 mrad is measured and is mainly correlated to the energy fluctuations of the driving pulse (~0.5% rms, [29]). When both WLG stages use the same nonlinear material and thickness, the intensity-to-phase coupling coefficients are very similar, and the relative phase noise can be as low as 32 mrad rms (single-shot, over 10k shots). When different materials or thicknesses are used, the phase noise increases but stays at low absolute levels around 65 mrad rms. The residual rms phase fluctuations are given for different WLG-stages in Tab. 1.

To explore the possibility of further extending the available seed bandwidth, we modified the experiment by driving one of the WLs with a 2080 nm, 100 fs pulse and the second WL with the second-harmonic (at 1040 nm) of this pulse (Fig. 9).

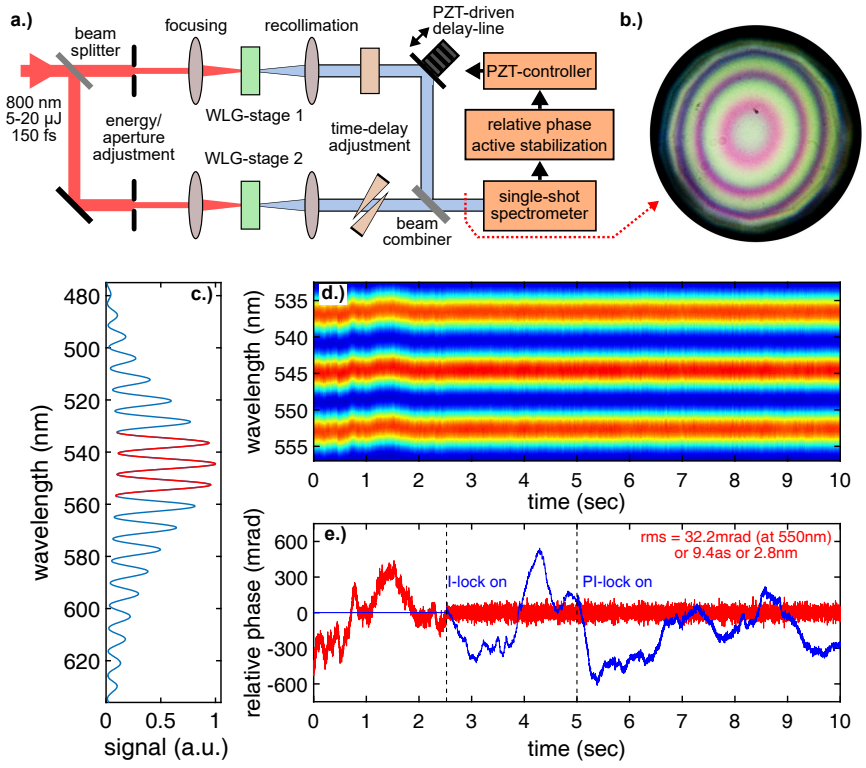

Fig. 8. Characterization of the phase-stability among separate white-lights. **(a)** Experimental white-light interferometer for the determination of the relative phase-noise among independent white-lights. An active stabilization-system eliminates temperature-induced drifts and interferometric noise. **(b)** Observed spatial fringes between the two white-lights at the red line marked in (a). **(c)** Coherent single-hot spectrum of spectra beating between two WLG sources with almost full fringe contrast (95% modulation). **(d)** Single-Shot interference trace (red marked section in (c)) without feedback till 2.5 s and with activated stabilization after. **(e)** Retrieved relative phase (red) and delay-line actuation (blue). Adapted from [37, 38].

Material 1	Material 2	Phase jitter (mrad rms (at 550nm))	Timing jitter as rms
2-mm YAG	2-mm YAG	32.2	9.4
3-mm sapphire	3-mm sapphire	41.6	12.2
3-mm sapphire	2-mm YAG	51.2	15.0
1-mm sapphire	3-mm sapphire	64.4	18.8

Table 1. Overview of relative phase noise (and the corresponding timing jitter) between two separate WLG if driven with 1 µm and in different materials and thicknesses. The lowest phase noise is achieved if both WL materials are identical in material and thickness.

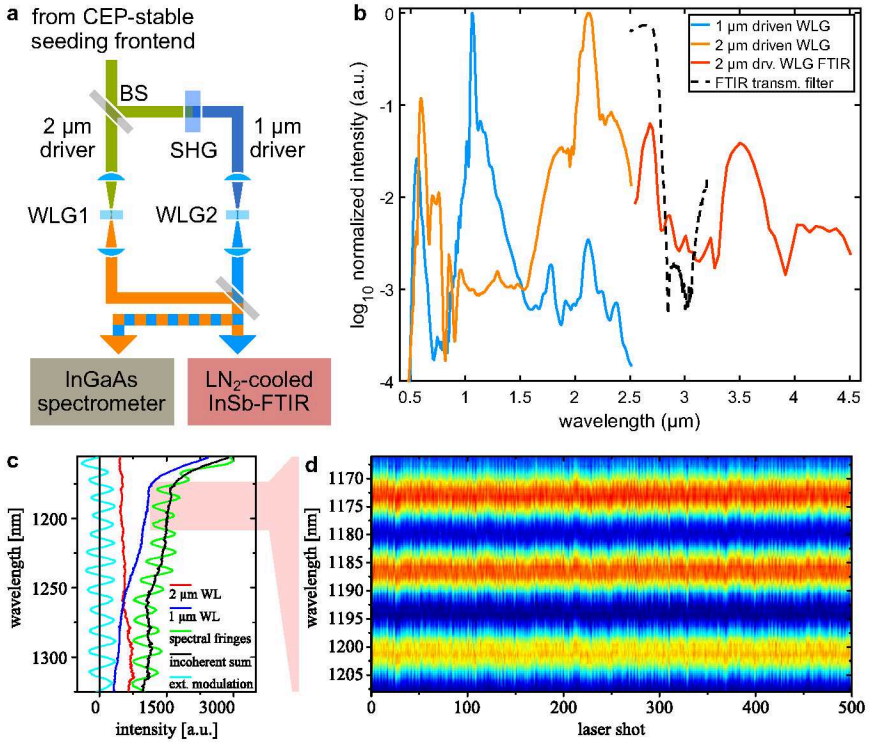

Fig. 9. **(a)** Setup for multi-octave wide seed generation via WLG driven by a CEP-stable pulse at 2 µm and its second harmonic. **(b)** Optical Spectra from WLG driven at 2 µm (orange/red) and 1 µm (blue) with few µJ of ~ 120 fs pulses in bulk media (YAG/sapphire). The spectra beyond 2.6 µm are measured with an Fourier transform infrared (FTIR) spectrometer using a cryo-cooled indium-antimonide-sensor (InSb) and a lowpass filter (dotted line). **(c)** Individual WL spectra as recorded with our indium-gallium-arsenide-based (InGaAs) spectrometer (red, blue), as well as the coherent sum exhibiting spectral fringes (green), the incoherent sum (black) and the extracted modulation (cyan). **(d)** Half-second long section of the interference trace, corresponding to 500 laser shots. Adapted from [37–39].

In this case, the relative phase stability and the absolute phase (with respect to the CEP of the seed driving pulse) are quantified. Remarkably, the two WLs exhibit good overall phase stability of 132 mrad rms, mainly deteriorating with respect to the previous case due to the additional intensity-to-phase coupling of the second-harmonic generation process involved. For reference, the energy fluctuations of the WLG driver were ~0.5% for the fundamental pulses and ~1% for its second harmonic.

These results have a few crucial consequences for parametric waveform synthesis: (I) there is the possibility to extend the PWS bandwidth by an additional octave in the mid-IR region; (II) a 60 mrad CEP fluctuation of the ~1 µm seeder pulse corresponds to an envelope shift with respect to the carrier wave of only 30 as (this will be relevant in Sec. 4.6); (III) it is possible to operate multiple phase-stable WLs with low phase-noise between each other; hence it is feasible to seed each synthesizer channel via a dedicated WL. The last point has a significant impact on the design of the PWS. The possibility of generating separate WL seeds for each spectral channel allows optimizing each of them in terms of spectral intensity/extension, phase, and intensity fluctuations. The seed spectral phase can also be individually optimized by choosing different crystals and thicknesses. Moreover, generating each WL close to the first OPA stage, helps to minimize the

WL mode degradation due to a shorter seed beam transport. The dispersion management scheme is also simplified since the dichroic beam splitters required to split a single seeding WL for the different spectral channels would introduce additional dispersion that needs to be compensated for afterwards. Fig. 10 illustrates the single-WL and multi-WL seeding schemes.

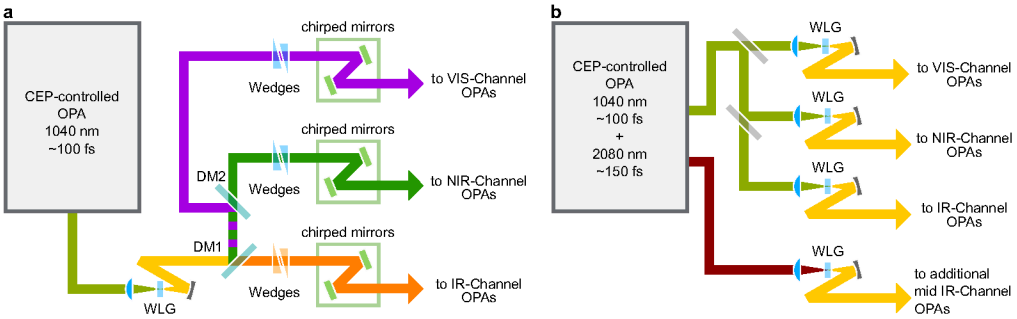

Fig. 10. Comparison between single-WL **(a)** and multi-WL **(b)** seeding schemes. The multi-WL scheme allows to cover a larger bandwidth by driving different WLs with different harmonics; simplifying the dispersion management and improving the beam quality of the seeding beam due to shorter propagation. Adapted from [31].

4.2. Narrowband OPA-seeder

As discussed in the previous section, the generation of a broadband and phase-locked seed relies on the WLG process. However, to generate a seed with stable CEP, the WL itself needs to be driven by a CEP stable pulse. In most cases, high-power laser amplifiers cannot be CEP-stabilized, or if so, they do not reach the stability necessary for pulse synthesis. For this reason, the generation of CEP-stable pulses via DFG appears to be the most reliable approach.

The simplest option is to make intra-band DFG from the pump laser pulse and if it is too narrowband by broadening it beforehand. However, this method can only produce a CEP-stable seed in the IR and mid-IR. Also additional nonlinear processes (e.g. second harmonic generation) would be needed to extend the seed in the visible and near-IR region. To control the CEP and further stabilize it, it would be necessary to introduce dispersion before or after the DFG stage. To avoid affecting the relative arrival time of the seed with respect to the pump in the following OPAs, an isochronic CEP compensator would be required [40].

Alternatively, the DFG can be utilized in a WL-seeded OPA. This approach allows to obtain a tunable CEP-stable seed pulse that can be further broadened via WLG. To achieve both shot-to-shot and also long-term stability, WL generation also requires driving pulses with excellent energy stability, a Gaussian beam profile, and preferably a pulse duration in the 50-300 fs range. In this section, we will present the main technical aspects of the implementation of our OPA-based seeder system.

Our seeder (Fig. 11) consists of a WL-seeded two-stage OPA, pumped with 800 nm and generating a signal at 1300 nm (idler at 2080 nm). Both stages, are based on BBO crystals (cut at 25.9°) and exploit the *Type-II oee* phase-matching geometry. In this configuration the signal and the idler pulses tend to walk away from the pump pulse in opposite directions inside the crystal, that is $\delta_{s-p} \cdot \delta_{i-p} < 0$ where $\delta_{j-k} = 1/v_{g_j} - 1/v_{g_k}$. The seed pulse is faster than the pump pulse and is timed such that it enters the crystal after the pump so that the two pulses overlap temporally after a short propagation. Once overlapped, the parametric amplification begins, and the generated signal and idler pulses remain locked to the pump pulse due to the gain. This interaction distance is much longer than both pump-signal and pump-idler pulse splitting lengths ($l_{s/i-p} = |\tau/\delta_{s/i-p}|$). Once the OPA-gain drops due to pump depletion, the three pulses separate

from each other because of the different group velocities and they cease to interact. By choosing the proper crystal length (in our case, 2.5 mm in the first stage, 4 mm in the second stage), it is possible to reach a condition for which the output signal and idler pulse energy depend neither on the input seed energy nor on the pump-seed arrival time difference fluctuations, but exclusively on the input pump pulse energy. In this OPA configuration, discussed for the first time in [41], the signal and seed pulse energy fluctuation can be as low as the pump one. As discussed in the

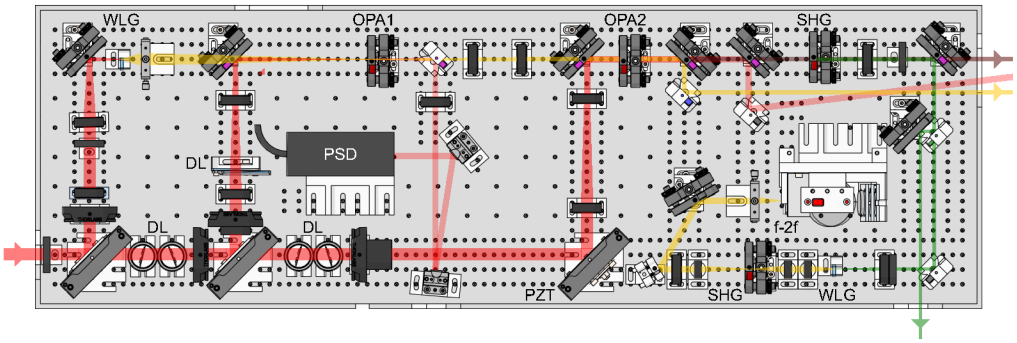

Fig. 11. Optical scheme of the CEP-stable OPA seeder. The 800 nm pump (in red) is split in three replicas, the first one driving the WLG (in yellow), the others pumping the first and second OPA stages (OPA1 and OPA2). The fist stage pump after amplification is directed to the pointing stabilizer detector (PSD), the corresponding actuators are placed outside the breadboard (not shown). Wedges act as optical delay lines (DL) in transmission and are used to fine tune the pump-seed delay in each OPA stage. The pump-seed delay in the second amplification stage (OPA2) can be actuated by the piezo-driven delay line (PZT), allowing for further active stabilization and control of the CEP of the idler beam. The CEP-stable idler (brown color) is frequency-doubled to obtain the 1040 nm CEP-stable pulse that drives the seed generation in the PWS spectral-channels. Its CEP is measured locally by means of an f-2f interferometer.

next section, the idler pulses generated with this OPA are passively CEP-stable. After the second stage, the idler pulses are separated from the pump and signal and frequency-doubled (in a *Type-I* BBO with 0.5 mm thickness to preserve beam quality at the expense of conversion-efficiency) to obtain 1040 nm pulses, whose wavelength is particularly suited for driving the WL seeds for the PWS. The broadband OPA amplifiers of the spectral-channels cover the 500-700 nm range (VIS-channel), the 650-1000 nm range (NIR-channel), and the 1200-2200 nm range (IR-channel), leaving a gap in the 1000-1200 nm region. Since the WL driver central wavelength was designed to be in this gap, the distorted regions of the WL spectrum around the pump wavelength are not utilized but only its spectral wings, which exhibit a smooth spectral intensity/phase.

After discussing the OPA scheme that minimizes energy fluctuations, we will briefly describe its technical implementation that plays a fundamental role in achieving stable long-term operation, excellent beam profile and high CEP stability. To achieve long-term stability, we minimized environmental effects on the setup such as temperature changes and air fluctuations. Reducing the beam path length within the optical setup and minimizing the number of reflecting optics in favor of transmissive ones helped to drastically increase the stability further. The compact Mach–Zehnder-type geometry (see Fig. 11) achieves these goals and further helps to keep the multiple pump beams roughly synchronized to the signal path. To minimize the effect of dispersion through the transmissive optics, we used SiO_2 optics, whose zero-dispersion wavelength ($\sim$1.3 µm) coincides with the central wavelength of the signal. To further reduce the environmental influences on the optical system, we implemented a temperature stabilized ($\sim$3 mK rms) breadboard, described in Sec. 5.2, and fully enclosed the setup including windows

for the input and output beams. In addition, a pointing stabilizer (TEM Messtechnik, Aligna) was added to fix the input pump beam direction with respect to the optical breadboard itself (position-sensitive detector (PSD) in Fig. 11).
The quality of the beam profile of the idler second-harmonic also plays a vital role, as the stability of the WL dramatically depends on it. Furthermore, the SHG pulses at 1040 nm have to propagate for a few meters before reaching the WLG stage of some of the spectral channels (as discussed at the end of the last section); therefore, to avoid diffraction, the beam profile needs to be Gaussian. To circumvent angular dispersion and achieve an excellent idler beam profile, we adopted a perfectly collinear OPA geometry and used custom dichroic mirrors (produced by Laseroptik) to combine and split the different beams.

4.3. Pump-seed timing effects on CEP for narrowband OPAs

We will now discuss how the idler CEP stabilization and control works in our OPA seeder. The so-called *passive* CEP stabilization occurring in OPAs was first observed by *Baltuška et al.* in 2002 [12]. This effect is explained by the fact that the idler pulse is generated during the OPA process by difference-frequency generation (DFG) between the pump pulse and the seed (signal) pulse. Provided that a replica of the pump pulse generates the seed pulse through a process that preserves the phase coherence (as for WLG), the shot-to-shot CEP variations of the pump will be coherently transferred to the seed pulse. Assuming that the pump-seed temporal overlap does not vary, the CEP fluctuations of the seed pulses are subtracted from the CEP fluctuations of the pump pulse, resulting in an idler pulse whose CEP is identical for every shot. However, in a real setup, the pump-seed temporal overlap in the OPA will fluctuate. The effects of pump-seed arrival time difference (ATD) fluctuations on the CEP of the idler pulse were studied in [13]. In this section, we will summarize the main results reported in that study concerning narrowband OPAs such as the seeder of our PWS.
The influence of a shot-to-shot pump-seed ATD variation named ΔT can be found analytically for the two extreme cases $\tau_{seed} \gg \tau_p$ and $\tau_p \gg \tau_{seed}$. When $\tau_{seed} \gg \tau_p$, the CEP variation of the idler is:

$$\Delta\Psi_i = -\omega_{seed}\Delta T, \tag{1}$$

otherwise, when $\tau_p \gg \tau_{seed}$, the CEP variation of the idler is:

$$\Delta\Psi_i = -\omega_p\Delta T. \tag{2}$$

Here ω_{seed} and ω_p are the central angular frequencies of the seed and pump pulses. Since in an OPA it is always true that $\omega_p > \omega_{seed}$, a temporal fluctuation ΔT will affect less the stability of the idler CEP if $\tau_{seed} \gg \tau_p$. This result also suggests that the idler CEP can be controlled by acting on the pump-seed ATD. In our OPA seeder (where $\nu_{seed} \approx 230$ THz), the idler CEP shifts by π for a $\Delta T \approx 2.2$ fs.
In light of the above, a 12 nm band-pass filter centered at 1300 nm is placed between the first and second stage of our OPA seeder. This filter narrows the bandwidth of the amplified signal emerging from the first OPA-stage such that $\tau_{seed} > \tau_p$ and also serves as a block for the first stage idler, preventing double seeding of the second stage. This helps to minimize the CEP noise induced by fluctuations of the beam paths in the OPA. A Pzt-DL (PZT in Fig. 11) consisting of a mirror mounted on a piezo-actuator is added to adjust the pump-seed delay in the second OPA stage, therefore allowing control over the idler CEP. The delay line is introduced in the pump beam path for convenience reasons. Our OPA seeder is also equipped with an f-2f interferometer and a spectrometer that allows single-shot CEP detection of the final output pulses at 1040 nm at the full repetition rate (see Sec. 5.1).

4.4. Broadband OPAs

In Sec. 4.1,4.2 and 4.3 we describe the key ingredients for the generation of multi-octave-spanning WL seeds with stable and controllable CEP. In this section, we discuss how to amplify the nJ-level seeds up to the mJ-level while preserving phase coherence. As mentioned in Sec. 3, the WL seed spectrum, which spans 2.5 octaves across the visible and IR range, can be amplified almost entirely by means of three different ultrabroadband OPA configurations. The ultrabroadband amplification bandwidth of all these OPAs is obtained via *group-velocity matching* of signal and idler pulses. In fact, when $v_{gs} = v_{gi}$, the first order term of the amplification bandwidth [2]:

$$\Delta\omega_G = \alpha|v_{g_i}^{-1} - v_{g_s}^{-1}|^{-1} + \beta|GVD_s + GVD_i|^{-\frac{1}{2}} + ... \tag{3}$$

tends to infinity (α and β contain OPA parameters). The group-velocity matching condition can be achieved both by *non-collinear OPA* configuration, as in the VIS channel, or by *degenerate OPA* configuration, as in the NIR and IR channels.

4.5. Pump-seed timing effects on CEP, broadband stretched/compressed OPAs

In Sec. 4.3, we discussed the effect of the pump-seed delay on signal and idler CEPs in a narrowband OP(CP)A, where the seed pulse is transform-limited (TL). In broadband OP(CP)As, as those implemented in the PWS spectral channels, the CEP dependency on pump-seed delay is quite different. In this case, the broadband seed pulse is usually stretched to fit the high-gain temporal window induced by the pump pulse (generally $\tau_p > 10 \cdot \tau_{seed_{TL}}$) and extract more energy from it. After amplification, the signal (or idler) pulses are compressed close to TL.
To describe the CEP dependency on the pump-seed delay analytically, we can extend the simple model developed in [13] to the chirped seed case. To do this we start with the seed pulse:

$$E_{seed_0}(t) = e^{-\left(\frac{t}{\tau_{seed_0}}\right)^2} e^{i(\omega_{seed}t+\phi_{seed})}. \tag{4}$$

The stretcher can be modeled in the frequency domain by multiplying the seed pulse by:

$$S(\omega) = e^{iGD\omega} e^{-i\left[CD\omega_{seed}+GD(\omega-\omega_{seed})+\frac{1}{2}GDD(\omega-\omega_{seed})^2\right]}, \tag{5}$$

where CD, GD and GDD are the 0$^{\text{th}}$, 1$^{\text{st}}$ and 2$^{\text{nd}}$ order dispersion of the stretcher. The seed pulse in time domain after the stretcher is then:

$$E_{seed_1}(t) = A_1 e^{-\left(\frac{t}{\tau_{seed_1}}\right)^2} e^{i\left[\phi_{seed}+(GD-CD)\omega_{seed}-\frac{1}{2}\arctan\left(\frac{2GDD}{\tau_{seed_0}^2}\right)\right]} e^{i\left(\omega_{seed}t+\frac{2GDD}{\tau_{seed_1}^2\tau_{seed_0}^2}t^2\right)}, \tag{6}$$

where $\tau_{seed_1} = \tau_{seed_0}[1 + 4(GDD/\tau_{seed_0}^2)^2]^{1/2}$ and A_N ($N = 1, 2, ...$) are suitable amplitudes.
We now assume that the signal pulse generated during amplification is a (higher intensity) copy of the stretched seed pulse multiplied by a shorter pump pulse ($\tau_{seed_1} > \tau_p$). In the opposite limit case ($\tau_p \gg \tau_{seed_1}$) it is trivial to show that the pump-seed delay has no effect on the signal CEP. If $\tau_{seed_1} > \tau_p$, the signal inherits the pump envelope, whose temporal peak (the arrival time) shifts according to the pump-seed delay T:

$$E_{s_0}(t) = A_2 e^{-((t-T)/\tau_p)^2} e^{i(\phi_{seed}+(GD-CD)\omega_{seed}-\frac{1}{2}\arctan(\frac{2GDD}{\tau_{seed_0}^2}))} e^{i(\omega_{seed}t+\frac{2GDD}{\tau_{seed_1}^2\tau_{seed_0}^2}t^2)}. \tag{7}$$

The CEP of the signal pulse is equal to the phase at the peak of its envelope, therefore at $t = T$:

$$\Psi_{s_0} = \phi_{seed} + (GD - CD)\omega_{seed} - \frac{1}{2}\arctan(2GDD/\tau_{seed_0}^2) + \omega_{seed}T + \frac{2GDD}{\tau_{seed_1}^2\tau_{seed_0}^2}T^2. \tag{8}$$

With respect to the narrowband TL case, where $\Delta\Psi_s(T) = \omega_{seed}\Delta T$, here the signal CEP gains an additional quadratic dependence on the pump-seed delay due to the second order dispersion (GDD).

Let's now see what happens once the signal pulses are compressed. To this end, we multiply the signal pulse (in the frequency domain) by $S(\omega)^{-1}$, which corresponds to a compressor ideally matched to the stretcher $S(\omega)$. Once back in the time domain, the signal pulse is:

$$E_{s_1}(t) = A_3 e^{-\frac{[4GDD^2T+(\tau_{seed_0}\tau_{seed_1})^2(t-T)]^2}{\tau^2_{seed_1}(16GDD^4+\tau^4_{seed_0}\tau^4_{seed_1}+4GDD^2(\tau^4_{seed_0}-2\tau^2_{seed_0}\tau^2_{seed_1})}} e^{iB}, \tag{9}$$

where B contains all phase terms. We can find the temporal position of the peak of the Gaussian envelope by looking where the argument of the exponential equals zero, that is for:

$$t_{peak} = \left(1 - \left(\frac{2GDD}{\tau_{seed_0}\tau_{seed_1}}\right)^2\right)T. \tag{10}$$

Substituting t_{peak} into the full expression of B in Eq. 9 we can finally obtain the CEP of the signal pulse after compression:

$$\Psi_{s_1} = \phi_{seed} + \left(\frac{\omega_{seed}}{R^2}\right)T + \left(\frac{2GDD}{\tau^4_{seed_0}R^4}\right)T^2, \tag{11}$$

where $R = \tau_{seed_1}/\tau_{seed_0}$ is the stretching (and compression) ratio. This expression allows us to observe that for large stretching ratios $\Delta\Psi_s(T) \to \phi_{seed}$. Because the condition $R \gg 1$ is fulfilled in any broadband OP(CP)A, this expression for signal CEP has general validity.

We conclude that the CEP of the signal pulse is not influenced by the pump-seed timing fluctuations, even when the stretched seed pulses are longer or similarly long with respect to the pump pulses, provided that the signal is later recompressed close to TL. In case of TL seed/signal pulses, that is for $R \to 1$, we recover the same expression found in [13] for the narrowband TL case with $\tau_{seed} \gg \tau_p$.

The same derivation can be applied to the idler pulse, with the difference that the idler carrier is given by the difference between the pump and seed carriers. For the idler pulse we obtain the following:

$$\Psi_{i_1} = \phi_p - \phi_{seed} + \left(\frac{\omega_i}{R^2} - \omega_p\right)T - \left(\frac{2GDD}{\tau^4_{seed_0}R^4}\right)T^2 = \phi_p - \omega_p\left(1 - \frac{1}{R^2}\right)T - \Psi_{s_1}, \tag{12}$$

where $\omega_i = \omega_p - \omega_{seed}$. Differently from the signal case, the pump-seed delay contribution to idler CEP after recompression does not vanish for large stretching ratios ($R \gg 1$):

$$\Psi_{i_1} = \phi_p - \phi_{seed} - \omega_p T, \tag{13}$$

in agreement with idler CEP expression (2) valid for $\tau_p \gg \tau_{seed}$. Consistently, when we consider narrow-band seed pulses without dispersion ($GDD = 0$ and $R = 1$), the Eq. 12 leads to Eq. 1, that was found for $\tau_{seed} \gg \tau_p$.

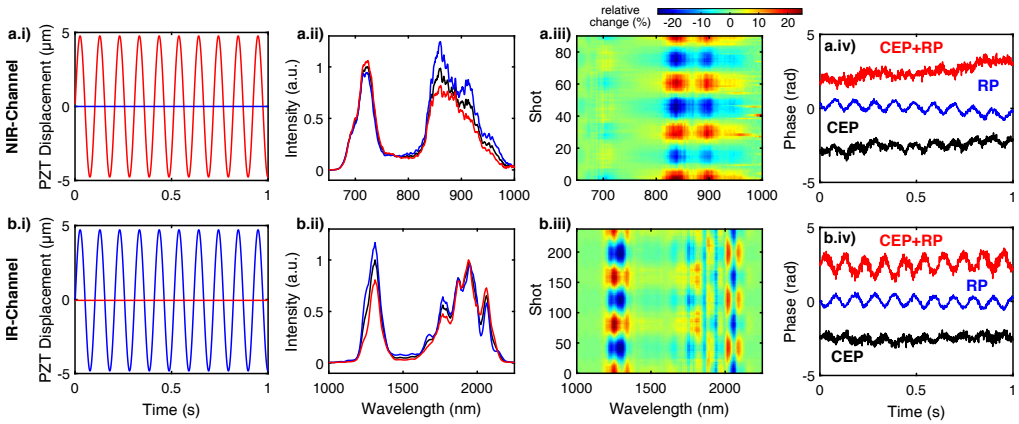

Fig. 12. Pump-seed ATD effects on the synthesis channels for **(a)** the NIR-channel and **(b)** the IR-channel. **(i)** Shows the sinusoidal ATD modulation with 60 fs_{pp}. **(ii)** Average spectra (black) and extrema of spectral modulation (red/blue). **(iii)** Trace of the spectral shift at the synthesizer channel output during pump-seed modulation. **(iv)** Effects on the measured phase of the relative-phase (RP, blue), the CEP+RP (red) and the CEP-effect (black) attained by subtraction.

As a practical example, we consider the influence of pump-seed temporal drifts on the signal CEP of the NIR channel in the PWS. In Equation 11 we substitute $R = 10$, $\omega_{seed} = 2.36 \times 10^{15}$ rad/s and $T = 1$ fs to the second term, while we can neglect the third term. This leads to a signal CEP shift (after compression) of 23.6 mrad for a 1 fs change in pump-seed arrival time difference. To experimentally verify this calculation, we induced a large change in the pump-seed delay in the OPA amplifiers of both the NIR and IR channel. The changes induced in the amplified spectra of both NIR and IR pulses are shown in Fig. 12 (a.ii, b.ii) and (a.iii, b.iii), while the corresponding phases are shown in Fig. 12 (a.iv, b.iv). The phase change is in the range of 1-1.5 rad for a ~60 fs delay, corresponding to 16-25 mrad for 1 fs, remarkably close to the value obtained from the previous model. In the last stage amplifiers of the PWS, we observed pump-seed shot-to-shot fluctuations < 2 fs rms, corresponding to small CEP changes. Larger drifts, up to ~10 fs, can occur over several tens of minutes, for parts of the setup that are not temperature stabilized, especially when opening (and leaving open) the PWS box. In the next section we will quantify the impact on the synthesized waveform of non-common mode CEP drifts among the two (and three) spectral channel pulses (see Fig. 13 & 14).

In conclusion, for the broadband OPA amplifiers in the spectral channels of the PWS it is not necessary to actively stabilize the pump-seed temporal jitter to maintain the CEP (and RP) stability. This statement is valid as long as: (i) we are interested only in the signal pulses from the spectral channels, and (ii) the pulses are utilized in the experiment once compressed. Both of these conditions are met in our PWS. This has interesting implications for next-generation OPCPA synthesizers. For instance, for a ≥1.5 ps pump duration and an $R = 100$ (assuming a 10 fs TL duration of the seed), a pump-seed jitter of up to 100 fs (peak-to-peak) would not significantly impact the CEP stability. In our PWS setup we implemented a slow-feedback that stabilizes the slow drifts (0.1-1 mHz bandwidth) of the pump-seed ATD in the last OPA stage, which can reach few tens of fs. This is mainly due to the thermalization of the external compressor (C2 in Fig. 7). These slow drifts have no impact on the CEP stability but lead to small shifts in the OPA output spectra. A simple stabilization scheme of the OPA spectrum is implemented by adjusting the pump-seed delay with piezo-driven delay-line placed in the pump paths of each last stage amplifier (Pzt-DL on the right bottom of Fig. 7). The error signal used to lock the spectrum is derived by the fluctuation of the center of mass of the output spectrum (with respect

to a reference spectrum), acquired every ~ 1 minute.

4.6. Basis set for stable and controllable waveform synthesis

So far, we have analyzed the effect of timing variations on the CEP of the narrowband OPA seeder and on the broadband OPA amplifiers. In summary, we concluded that: (i) the pump-seed delay in the seeder DFG stage can be efficiently exploited to control the CEP of the seeding pulses; (ii) the pump-seed delay jitter in the PWS spectral channels influences the CEP of the compressed output pulses only insignificantly. The pulses from the spectral channels are then coherently combined to form the final waveform. We will now discuss the most effective way to control the synthesized waveform by finding the best set of waveform parameters and the most convenient way to observe and control them.

In a parallel parametric waveform synthesizer, the synthesized waveform is obtained by superimposing two or more pulses covering different bands of the optical region. In our PWS, the pulses to be synthesized cover 520-700 nm (VIS-channel, under development), 650-1000 nm (NIR-channel), and 1200-2200 nm (IR-channel). If we assume that (i) the pulses have a stable spectrum and energy (negligible shot-to-shot fluctuations) and that (ii) the pulses are a superposition of plane waves propagating along the same direction neglecting transverse properties (will be discussed in Sec. 6), then the synthesized electromagnetic field waveform depends on: (i) the spectral phase of each pulse, (ii) the CEP of each pulse and (iii) the arrival time (AT) of each pulse. The complexity can be initially reduced by considering the spectral phase of each building pulse as fixed, since most applications require them to be fully compressed. Given the N pulses to be synthesized (that is, a PWS with N spectral channels), we would need to know N CEPs and N ATs. This adds up to $2N$ synthesis parameters in total. However, since a common shift in arrival time of the N pulses does not affect the synthesized waveform, we can consider one of the N pulses as a reference and express the properties of the remaining $N-1$ pulses as differences with respect to the reference pulse. The reference pulse is hence called the *master pulse*. This leads to $N-1$ ATDs with respect to the master pulse.

Let us now call CEP_1 the CEP of the master pulse. Similarly to what we did with the ATs, the CEPs of the $N-1$ pulses (the *slave pulses*) can be equivalently expressed by relative phases (RP_{12}, ..., RP_{1N}) and ATDs with respect to the master pulse CEP and AT. The synthesis parameters are now $2N-1$: CEP_1, $N-1$ RPs and $N-1$ ATDs.

Let us assume that we have full control over the CEP of the master pulse (CEP_1). We can now investigate the effects of ATDs and RPs on the synthesized waveform. To this end, we consider the synthesis of two pulses, pulse 1 being the master pulse and pulse 2 being a slave pulse. The behavior of the synthesized waveforms is shown in Fig. 13, where we set CEP_1 (IR channel) to a fixed arbitrary value and varied either ATD_{12} or RP_{12}. In the first case (plots a,b) the ATD_{12} changes by 0.67 fs, corresponding to $\pi/2$, while RP_{12} stays fixed (therefore CEP_2 changed by $\pi/2$). In the other case (plots c,d) the RP_{12} changes by 0.67 fs, corresponding to $\pi/2$, while ATD_{12} stays fixed (therefore also in this case CEP_2 changed by $\pi/2$). Small RP changes ($\Delta RP_{12} \ll 2\pi$) result in significant changes of the synthesized waveform. On the contrary, ATD variations that are small with respect to the duration of pulse 2 ($\Delta ATD_{12} << \tau_2$) do not significantly influence the synthesized waveform. This implies that a change in CEP_2 does influence the synthesized waveform only if it is accompanied by a change in RP_{12}. These simple observations suggest that RP is a stronger synthesis parameter with respect to the $CEP\&ATD$ pair. Therefore, the $2N-1$ synthesis parameters can be reduced to just N parameters, that is CEP_1 and $RP_{12}, ..., RP_{1N}$. This allows us to tremendously simplify the waveforms control and stabilization system. This simplification entails a small decrease in the design freedom for the waveform, that however is insignificant in the present state. To prove this, the maximum waveform difference attainable by controlling the additional degree of freedoms in a three channel synthesizer ($CEP_1 + RP_{12} + RP_{13}$ only vs. $CEP_1 + CEP_2 + CEP_3 + ATD_{12} + ATD_{13}$) is shown

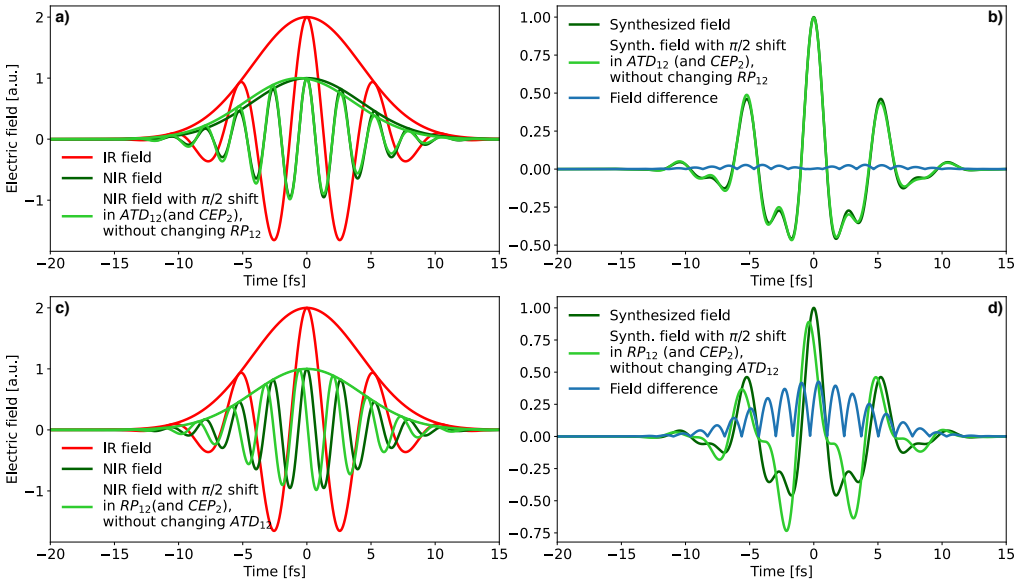

Fig. 13. **(a)** Electric fields of IR (red) pulse (1), NIR pulse (2) with $ATD_{12} = 0$ (dark green) and NIR with $ATD_{12} = \pi/2$ (light green). **(b)** Synthesized fields with and without ATD_{12} shift together with electric field difference (blue). **(c)** Electric fields of IR (red) pulse (1), NIR pulse (2) with $RP_{12} = 0$ (dark green) and NIR pulse with $RP_{12} = \pi/2$ (light green). **(d)** Synthesized fields with and without RP_{12} shift together with electric field difference (blue).

in Fig. 14 in the limit case of $\Delta CEP_2 = \Delta CEP_3 = \pm\pi$ for two different arbitrary waveforms (different RP_{12} and RP_{13} setpoints).

In both cases, the additional freedom granted by the CEP_2 and CEP_3 control allows only for small modifications to the synthesized waveform, showing a maximum field difference of $< 10\%$. It is worth noticing that the waveform variations are also very small because we chose the IR channel to be the master channel, which contains most of the overall energy. This is the optimal choice for this type of stabilization scheme. If the energy of the different building pulses were similar, the variations on the synthesized waveform due to ATD fluctuation would be slightly larger, but still negligible in most applications.

The possibility of attaining extensive control over the synthesized waveform through the N parameters set instead of $2N - 1$ allows for a significant simplification of the active waveform control system, resulting in less detectors and fewer actuators. Moreover, it is also important to anticipate that the measurement noise associated with RP measurements is significantly lower than that associated with both ATD and CEP measurements since the latter usually require multiple nonlinear processes each (e.g., f-2f for CEP, a cross-correlation in the balanced optical cross-correlator for ATD), while the RP can be measured in a linear fashion (via spectral interference) or at most via a single nonlinear broadening stage (e.g., mild spectral broadening). Together with a simpler measurement setup of the synthesis parameters, the control of $CEP_1 + RP_{12}$ ensures superior stabilization performances compared to the control of $CEP_1 + CEP_2 + ATD_{12}$ in our current 2-channel system. This statement will be proven in later sections when we will look at active stabilization results (see Sec. 4.7 and 7).

Now that we have defined the synthesis variables, that are CEP_1 and RP_{12} (RP_{13} will be added in future works with the third spectral channel), let us discuss how to control them. In Sec. 4.3 we already showed that the CEP of the idler pulses of the OPA-seeder can be efficiently controlled

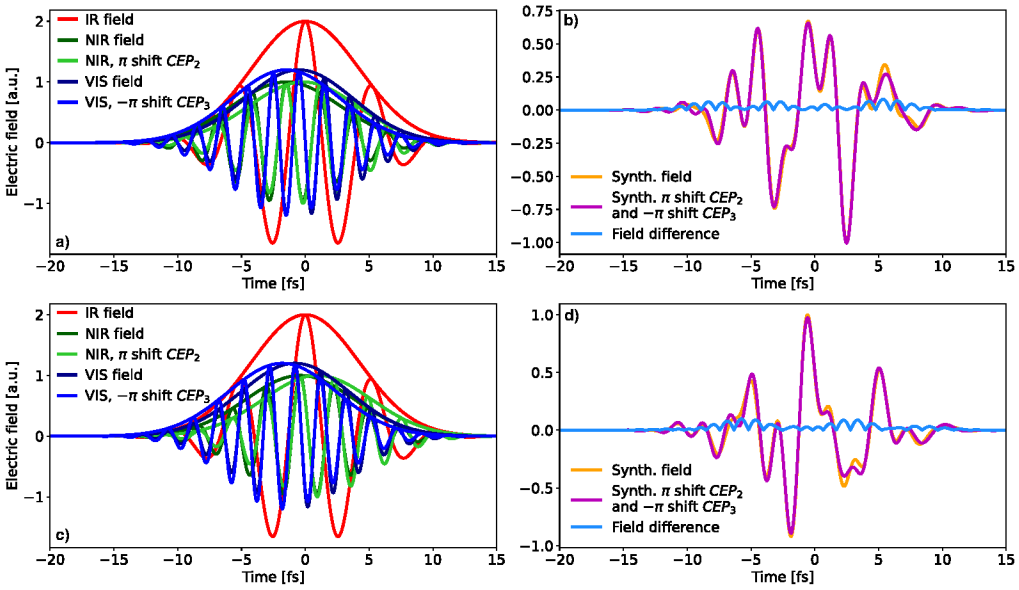

Fig. 14. **(a)** Electric fields of IR (red) pulse (1), NIR pulse (2) with $CEP_2 = 0$ (dark green) and with $CEP_2 = \pi$ (light green), VIS pulse (3) with $CEP_3 = 0$ (dark blue) and with $CEP_3 = \pi$ (light blue). **(b)** Corresponding synthesized fields with and without $CEP_{1,2}$ shifts, together with electric field difference (blue). **(c)** Same as (a) for different $RP_{1,2}$ setpoints. **(d)** Corresponding synthesized fields with and without $CEP_{1,2}$ shifts, together with electric field difference (blue).

via a Pzt-DL in the beam-path of the pump (or of the seed). In principle, having the Pzt-DL on the signal path is better since, in this case, the CEP stabilization would not affect the ATD of the CEP-stable idler, whose temporal overlap (after WL generation) is necessary for the following OP(CP)As. However, this effect is minuscule since the Pzt-DL need to move only a couple of fs during active stabilization, thanks to our compact OPA design. According to Eq. 1, a 2π CEP shift can be attained with a delay of ≈ 4.3 fs, a small amount compared to $\tau_{pump} \approx 150$ fs. Practical considerations led to placing the Pzt-DL in the pump path of the second stage, as shown in the OPA scheme in Fig. 11. Indeed, adding a delay-line on the signal path (between first and second stage OPA) would require adding more optics to the otherwise very compact Mach–Zehnder-type setup.

The idler pulses from the OPA-seeder drive the WLG stages that create the seeds for each spectral channel of the PWS. Since the WLG process is coherent (as quantified in Tab. 1), we can control the CEPs of the seed pulses by acting on the idler's CEP. Moreover, in Sec. 4.3 we concluded that the CEP stability of the seeds is maintained during their amplification in the spectral channels without the need for active stabilization of the pump-seed ATDs. Therefore, by controlling the idler CEP in the OPA-seeder, it should be possible to control CEP_1, the CEP of the *master channel output*. Stabilization and control of RP_{12} can be obtained by using a Pzt-DL in the beam path of either the master or the slave pulse. In our PWS, we decided to use two delay lines instead of one. By doing so, we could use the first delay-line to stabilize fast RP_{12} fluctuations with a short-range actuator, while the second delay-line is used to control RP_{12} over an extensive range spanning hundreds of optical cycles. In order to achieve a high stabilization bandwidth, the first delay-line consists of a home-built short travel range piezo-driven actuator (identical to the one used in the OPA-seeder) actuating a 1-inch mirror that was placed on the signal path of the slave channel ($\sim 0°$ incidence) before the last stage amplifier (see Fig. 7). Alternatively, this

Pzt-DL could be placed after the last-stage amplifier. These two options are equivalent in terms of waveform control, and the first was chosen for practical reasons. Instead, the second delay line is based on a commercial translation stage with position feedback (PI, N-565.260), which allows for a long-range and nanometric precision, also beneficial to quickly scan or adjust the time-zero between the master and slave pulses.

One more Pzt-DL was added in the beam-path of the pump pulse of the last stage amplifier of each spectral channel (both master and slave). As discussed, the pump-seed delay in the spectral channels does not significantly influence the CEP of the amplified signal pulses, provided that they are used once temporally compressed. However, particular applications might require waveforms with specific chirp profiles [42]. In this case, it might be necessary to additionally stabilize the pump-seed ATD in the last stage amplifiers (the booster stage) since the corresponding pump pulses undergo a completely separate beam path (see Fig. 7), leading to a few fs temporal jitter with respect to the signal pulses. Moreover, as outlined in Fig. 12, the spectrum of signal pulses emerging from each spectral channel depends on the pump-seed delay; therefore, remote control allows for easy optimization. As mentioned at the end of Sec. 4.6, these delay lines were recently used to stabilize the spectral shape of the OPA outputs, that can undergo small and slow (<1 mHz) drifts due to thermalisation dynamics occurring in the external compressor (C2 in 7) and influencing the pump-seed delay in the last OPA stages.

The control system designed to stabilize and shape the synthesized waveforms by driving the aforementioned Pzt-DLs will be presented in Sec. 5.1. In the last part of this section, we describe the multi-phase detector that allows to measure the CEP_1 and RP_{12}.

4.7. Dual in-line phase meter

In the previous chapters, the most effective synthesis parameters were defined (RP_{12} and CEP_1), and suitable locations for the corresponding actuators were identified. The measurement of synthesis parameters serves a twofold purpose: (I) stabilization of the multi-path interferometric setup within the PWS and (II) control of the final synthesized waveform, with resolution down to a fraction of the period of the optical cycles. The measurement of RP_{12} and CEP_1 should preferably occur after the individual pulses have been recombined, so that no additional temporal jitter is introduced afterward. For this purpose, the final beam combination optic(s) (see DM1 and DM2 in Fig. 7) were designed to provide a replica at the secondary port with 5 % of the input pulse energy. To avoid possible drifts among the two synthesis parameters, a unique all-inline multi-phase meter capable of simultaneous detection of RP_{12} and CEP_1 was developed [43] (see Fig. 15). The basis of this phase meter is spectral interferometry, where spectral beats need to be created by nonlinear conversion(s) to retrieve the CE and relative phase. In our current case, the spectrally non-overlapping NIR and IR-channel pulses require a linear spectral beat (f_1-f_2) in order to retrieve the relative phase RP_{12}. For this purpose, a mild self-phase-modulation-based broadening in bulk is exploited to spectrally broaden the short-wavelength wings of the IR-channel pulse and create the desired spectral overlap with the NIR-channel pulse around 950 nm. To selectively apply the broadening via self-phase-modulation to the IR pulse only and avoid other RP-dependent cross-sensitivities (such as cross-phase modulation) that might appear in such an in-line scheme, the NIR-channel pulse is attenuated and delayed before both pulses are focused into a few mm of YAG acting as broadening-stage. Refocusing of the beam in a subsequent stage for second harmonic generation additionally creates an (f_2-$2f_1$) beat between the frequency-doubled long-wavelength leg of the IR-channel pulse and the NIR-channel pulse, which is proportional to both RP_{12} and CEP_1. The second harmonic generation produces not only this inter-pulse f_2-$2f_1$ beating but as well an intra-pulse f_1-$2f_1$ beating. Such inter-pulse CEP-detection brings the disadvantage of being sensitive to RP_{12} too; on the other hand, it offers a higher signal-to-noise ratio with respect to the intra-pulse CEP detection. Moreover, since the

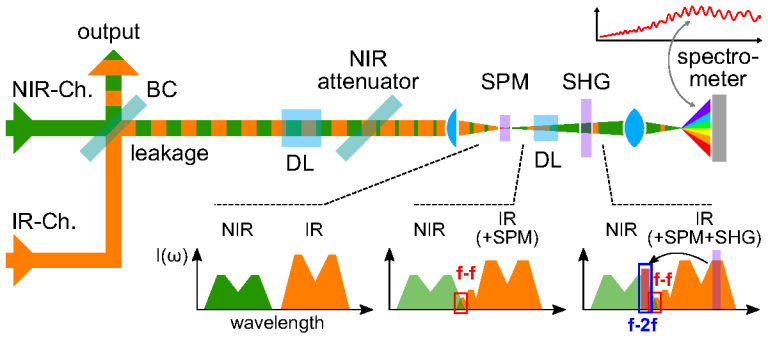

Fig. 15. Scheme of the dual-phase meter. The secondary output from the NIR/IR beam-combiner is used for CEP/RP detection. First the temporally overlapping NIR and IR beams are delayed (DL) by simple dispersion, then the NIR is attenuated before focusing into an self-phase-modulation stage to predominantly broaden the IR-component. After a second delay element the beam is refocused into an stage for second harmonic generation for 2f generation to enable CEP detection. Afterwards all beams are projected onto the same polarization plane and are observed by a single-shot spectrometer. Adapted from [38].

RP can be stabilized with really low residual noise, this does not negatively impact the CEP stabilization performance. The delays among the replicas of the NIR pulse, the IR pulse and the second harmonic of the IR pulse used in the multi-phase meter correspond to the spectral beat frequencies detected on the spectrometer. To have the beat frequencies well separated and not too close to zero-frequency, the delays can easily be adjusted by inserting suitable dispersive materials in between the nonlinear optical components or by exploiting different polarization states in combination with birefringent materials. Finally, all signals are projected onto a common polarization plane with a wire-grid polarizer and observed by a custom-made single-shot spectrometer (see Chapter 5.1). The spectral regions in which the different beating signals are observed can be superimposed (e.g. SHG_{IR}, SPM_{IR}, NIR-channel) and can be observed by the same spectrometer to use the optical energy efficiently. The only requirement to retrieve the corresponding phases is that these spectral beats appear at different beat-frequencies. A Fourier transform of the observed optical spectrum exhibits magnitude signals at those beat frequencies. Tracking and unwrapping the phases of those Fourier components allows to isolate the desired signals associated with synthesis parameters, which then can be used to generate the error signals for the active stabilization system of the PWS, as shown in Fig. 16). We observe a low phase noise for the RP measurement, which involves self-phase modulation only, and higher noise for the CEP measurement, which additionally requires second harmonic generation, which introduces substantial intensity-to-phase coupling. While the WLG-based RP measurement can yield as low as 30 mrad rms of measurement noise (see Tab. 1), the second harmonic generation for CEP detection adds 150-200 mrad of measurement noise on top of the noise of the source.

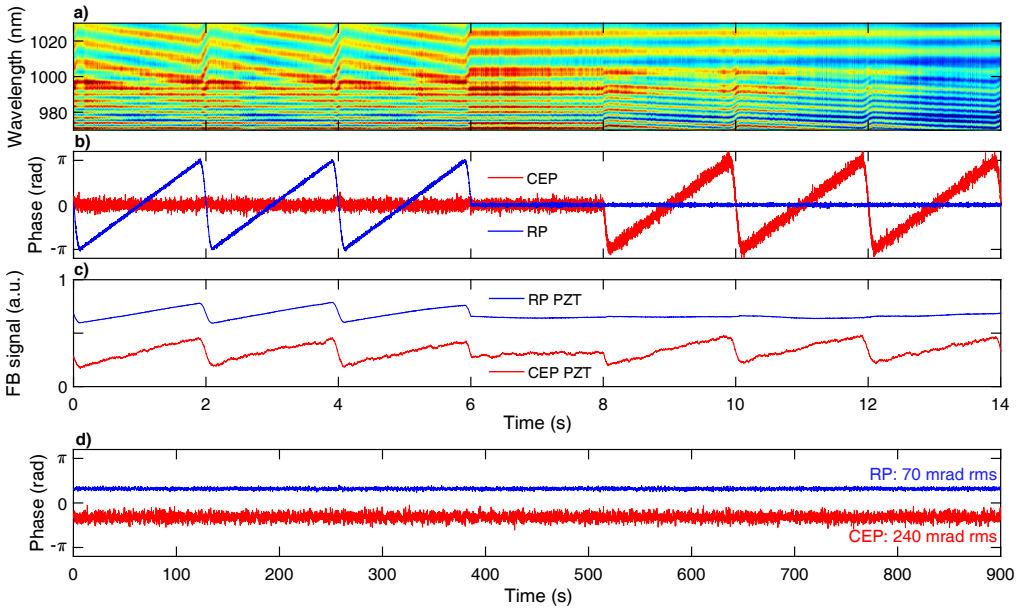

Fig. 16. Dual Phase Meter Measurement: **(a)** Trace of observed spectral fringes with superimposed beats for CEP and RP detection. **(b)** Extracted CE-phase in red and RP values in blue. A locked triangular RP scan is performed (0-6 s) and moved the both the RP and the CEP-actuator (in **(c)**) due to the CEP-RP convolution, in order to keep the CEP itself stable. A triangular locked CEP-scan (8-14 s) only moves the CEP-actuator. **(d)**) Locked CEP and RP with remaining phase noise of 70 mrad (RP) and 240 mrad (CEP). Our control system stabilizes both phases and allows to manipulate the synthesis set points. Adapted from [7].

5. Technical implementation

One of the most significant challenges to achieve stable synthesis with a parallel synthesizer scheme is to realize an optomechanical setup with sufficiently high passive stability and implementing an active timing stabilization with high bandwidth and reliability. While the nonlinear optics techniques to achieve and maintain phase-stable pulses and measure them were discussed previously, now a focus will be on the low-latency control system and the optomechanical implementation of the PWS setup.

No matter what the capabilities of the active stabilization system are, the optical setup should exhibit the lowest possible phase drifts already in passive operation. This goal can be achieved partly by selecting the correct means of pulse generation, amplification and phase detection methods as previously laid out. Additionally, the interferometric setup needs to be realized with high precaution to avoid long-term drifts or (undamped) vibrations of the optical elements, affecting the phase stability and the beam pointing.

5.1. Active phase stabilization and control system

The basis of the optical means to gain access to the relevant timing parameters was previously discussed with the introduction of the multi-phase meter for detecting the CEP and RP values. Phase measurement techniques are favored over other envelope timing tools such as balanced optical cross-correlators (BOC, [44]) for our application since phase changes have a much greater impact on the synthesized waveform compared to envelope arrival time changes. Moreover, the

in-line phase measurement is less prone to thermal drifts and more robust with respect to pointing changes and beam profile changes. On the other hand, the balanced optical cross-correlator can measure an absolute timing relation between two pulse envelopes, while a phase measurement can only determine relative phase changes with respect to the previous measured state. If a phase difference greater than π occurs between two consecutive measurements (*phase-jumps*), the relative change will be ambiguous and the phase-lock will be void. In this case, the synthesized waveform changes in an unknown direction and, if a waveform scan is being performed, it can no longer be brought into relation to previously synthesized waveforms. This ability is crucial during a full CEP-RP scan, for example, to study the generated high-harmonic emission [8], or when keeping a fixed set-point during an attosecond streaking measurement.

This circumstances leads to the conclusion that a scheme based on phase measurements practically requires a pulse repetition rate of >100 Hz and, if possible, a single-shot and every-shot evaluation of the spectral interference. Out of these demands, we developed a dedicated spectrometer based on a field programmable gate array logic (FPGA). The FPGA processes the data of a linear image sensor (Hamamatsu, S10453 (<1.1 µm), G9208-256W (1.2-2.3 µm)) within our spectrometer with low latency and on an every-shot basis at 1 kHz rep.-rate. The FPGA computes the necessary Fourier transforms and determines the unwrapped phase information within a few hundred μs from the recorded spectra to provide sufficient time for the feedback system to move the piezo-driven delay-lines accordingly and to compensate for the observed drifts with only 1-2 laser shots of latency. Besides these single-shot phase tracking spectrometers, an FPGA-based feedback system was implemented for calculation of the individual feedback signals to actuate the corresponding piezo-driven delay lines (see Fig. 17). This control system features phase-unwrappers with error detection, normalization calculation (for BOCs), frequency response filters (via finite impulse response (FIR) filter), a feedback matrix for orthogonalization, range-limiters and arbitrary waveform generators. For actuation, we implemented fast acting

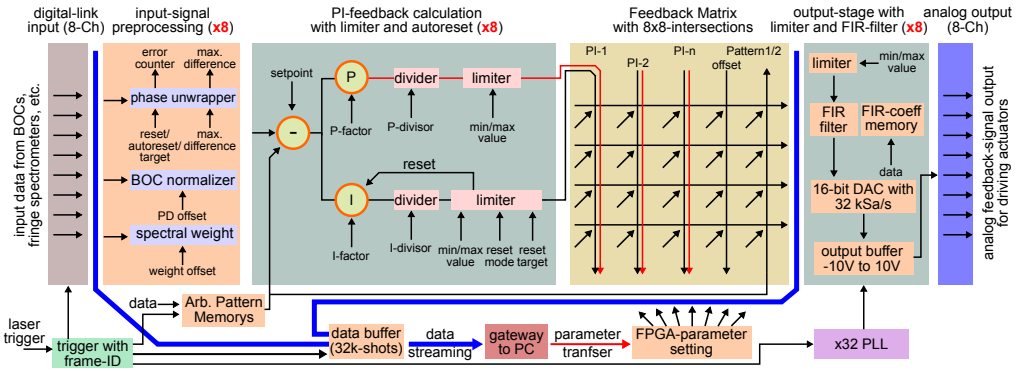

Fig. 17. Overview of the FPGA-based feedback system. Incoming timing parameters are preprocessed such as unwrapping for phase-values or normalized balancing for BOC-inputs. Then the processed observables enter a PI-controller section before a matrix allows to (de)couple the individual feed-backs and derive a suitable control signal to the multiple timing actuators (fast and slow). With this system, the laser pulses are indexed and all input/output parameters are recorded to maintain a full insight on the synthesizer state at any given time. Adapted from [38].

(400 Hz bandwidth) and low range (3 µm) piezo-driven ring actuator (Noliac, NAC2125-A01) moving 1-inch mirrors. In the CEP-stable front-end we can control the overall CEP with this actuator over a few cycles, which is sufficiently wide due to its 2π periodicity. An additional ring-piezo actuator is placed before the 3rd stage OPA of the NIR-channel to control the RP. Additionally, we use a 25 mm long-range stick-slip stage (PI , N-565.260) to adjust the rough

phase-delay, respectively the temporal separation between the NIR and IR pulses. The feedback system allows configuring the phase set-points, the proportional and integral feedback parameters and the coupling coefficients. Via scripts executed on a control computer, we can also perform parameter scans of the waveform with different patterns, such as a sinusoidal, a linear ramp or a step function (see Fig. 18). We obtain a data stream from the control system containing

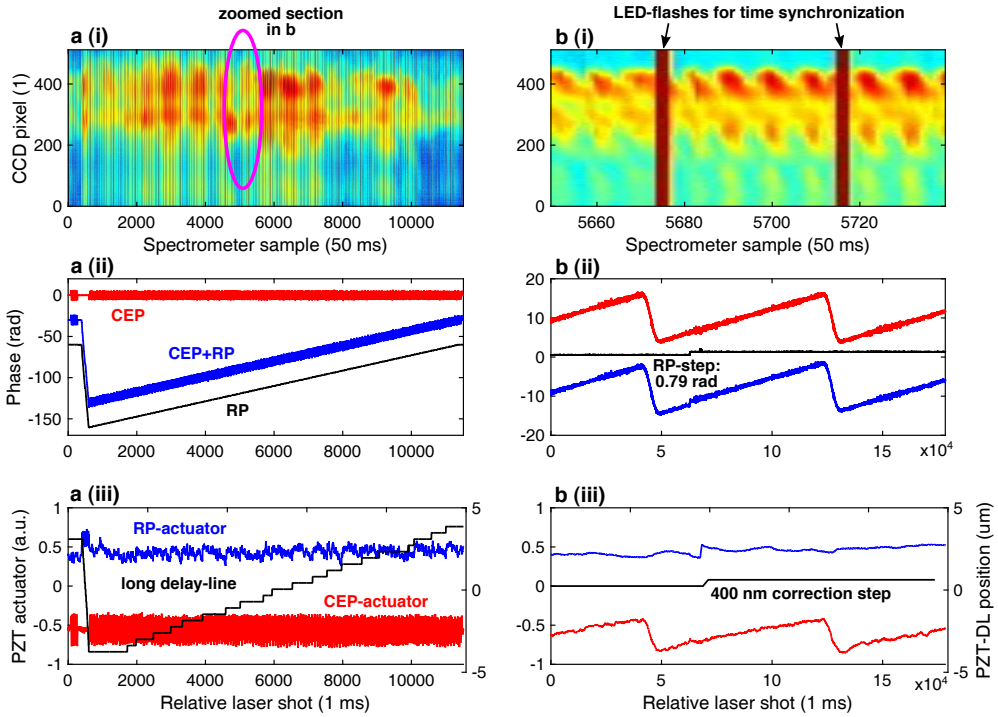

Fig. 18. Exemplary trace of a synthesized waveform scan with measured experimental observable in **(a)** and zoomed-in section in **(b)** for one scan-cycle. The observable **(i)** are here raw HHG-spectra (50 ms integration time). **(ii)** Measured phase observables where the RP follows a plain ramp and CEP is driven as a saw-tooth modulation for a full 2D parameter mapping. **(iii)** Corresponding actuator signals for the CEP-actuator (red) RP-actuator (blue) and a long-range stage with correction steps (black), to keep the short-range actuators in their dynamic range.

all input and output parameters for each indexed laser pulse so that other data recorded in parallel (e.g. HHG-spectra) can be fully synchronized with corresponding RP-CEP values in post-processing. In this mode, highly efficient and flexible data acquisition is achieved since additional experimental data can be collected without dead-time.

A complete reconstruction of the synthesized waveform can be recorded by an attosecond streaking trace, allowing to determine the absolute value of the RP between the individual sub-pulses and their CEPs numerically. By splitting the spectrum of the waveform obtained from the streaking trace and normalizing its spectral intensity to that measured with an optical spectrometer, one can obtain a quite accurate reconstruction of the electric field of each pulse. The spectral phase can then be compared with the measurements using two-dimensional spectral shearing interferometry (2DSI) to check for consistency. After this procedure, if the synthesis parameters are scanned, the corresponding waveforms can be derived numerically by applying the relevant CEP and RP offsets.

5.2. Opto-mechanical setup

The passive stability of the optical setup is of paramount importance to achieve stable synthesis. To reduce phase and pointing fluctuations, the number of reflections and the beam path of the setup need to be minimized. Due to the complexity of the PWS setup, we opted for a modular design, where each module was individually optimized. The different modules are: the CEP-controlled seeder, the dual-beam delay lines (next to the seeding front-end in Fig. 7), the spectral channels and the multi-phase meter. Each module is implemented on an individual 5 cm thick custom-made aluminum breadboard resting on a 4 mm thick silicone rubber mat placed directly on the optical table. The silicone rubber helps to even out the weight distribution and avoid bistability (see Fig. 19). Air fluctuations are effectively prevented by enclosing each module. While the seeder module is fully sealed by using anti-reflection-coated windows for the beams to propagate in or out, the broadband spectral channels have holes at the beam output to avoid additional dispersion and possible nonlinearities. Most optomechanics are also custom designed and milled from aluminum (see Fig. 19c). On the one hand, this allows achieving a $\sim$ 3 times higher density of optical components with respect to conventional optomechanics, granting the possibility to significantly shorten the beam path and the footprint of the setup. On the other hand, the custom components were designed to have only the necessary degrees of freedom (most mirrors do not have any adjustment screw), enabling significantly higher passive stability, which simplifies the alignment procedure. The optics are fixed by spring-loaded levers or ultraviolet-cured glue instead of a regular top-screwing mechanism to avoid stresses that would deteriorate the phase front of the pulse. Another critical aspect of the optomechanical setup is temperature stabilization. Temperature fluctuations in the environment lead to deformation of the optomechanics resulting in pointing and length changes of the beampath. We observed that these changes are reversible for minor air temperature variations ($<$ 1 K) but non-reversible when large temperature changes persist for tens of minutes or longer. To decouple the PWS setup from environmental influences, an active temperature stabilization system is implemented on each breadboard. Unlike laser amplifiers, where a significant amount of heat has to be removed due to the quantuum-defect, the modules of the PWS are OPA-based and thus without any significant heat load. This allowed us to avoid water-cooled breadboards that would require noisy chillers and pumps that could potentially introduce vibrations due to the water flow and decrease the overall reliability of the setup. Instead, we use electric heaters to temperature stabilize the breadboards of each module. On the surface of each breadboard, 8 high precision

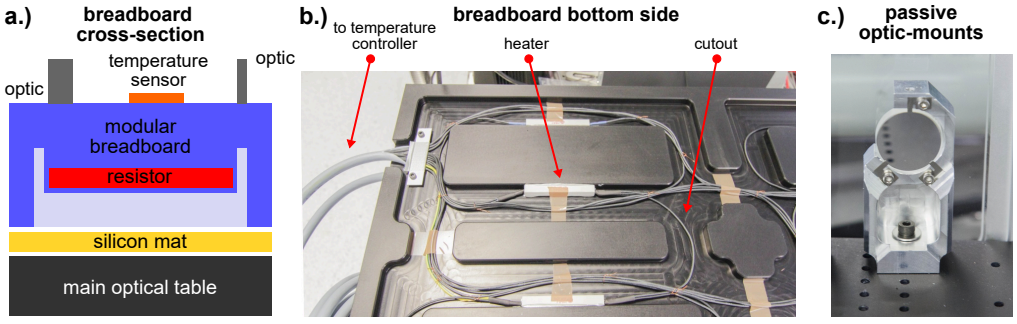

Fig. 19. Details on the opto-mechanical implementation: **(a)** Layering of the breadboard modules. **(b)** View of the bottom of the breadboards with vibration free heating elements for multi-zone temperature stabilization. **(c)** Highly stable custom-made optic mounts holding the optic either via springs or via ultraviolet-cured glue. Adapted from [38].

sensors (Pt-1000) measure the temperature of different zones. On the bottom of the breadboard, 16 resistors, grouped by 2 and placed in specific cut-outs, are used to stabilize the temperature of

each zone individually by having a set-point of 2-3 K above room temperature. The set-point is chosen to be slightly above the maximum temperature we usually experience in the laboratory when the air conditioning malfunctions. Thanks to these temperature-stabilized breadboards, our seeder achieves an out-of-loop temperature stability of 3.3 mK rms over the course of several months, eliminating this environmental influence and the associated misalignment.

6. Spatial properties and beam combination

Pulse synthesis requires not only the temporal superposition between constituent pulses, but also their spatial overlap. Moreover, the full spatiotemporal overlap requires shot-to-shot and long-term stability to guarantee highly reproducible synthesized waveforms. The spatial overlap of all constituent pulses requires characterizing the evolution of each beam profile along the propagation axis. This characterization allows us to evaluate the beam quality but also to ensure each pulse reaches its focus at the same longitudinal position after a common focusing element. By doing so, it is possible to estimate the corresponding intensities and the intensity ratios between the pulses of each channel at the interaction point (usually close to the focus). The intensity ratio particularly impacts the shape of the synthesized field, therefore playing a significant role in nonlinear light-matter interaction. Moreover, non-linear processes that require phase matching, such as HHG, are highly dependent on the beam waist at the focus, and its corresponding Rayleigh length [45]. Consequently, combining constituent beams with similar Rayleigh lengths (different focus sizes) or similar focus sizes (different Rayleigh lengths) can strongly affect phase-matching. The reason is that, in each case, the intensity ratio and relative phase between the beams evolve differently across the focus. In the current PWS, the beam sizes in focus were matched, meaning that the far-field beam waist ratio between the IR and NIR channels is ≈ 2. The spatial characterization of the PWS is challenging, as the output covers 1.7 octaves of spectral bandwidth, and beam cameras capable of capturing the entire bandwidth are currently rather expensive. In addition, for many nonlinear, strong-field experiments, tens of micrometer of focus diameter are typically necessary, and pixels that are small enough to resolve such beam dimensions are unfortunately only standard in silicon (Si)-based detectors, which are only spectrally sensitive up to $\approx 1\mu$m. Fig.20 (a-b) shows the far-field NIR and IR beam profiles after beam combination. The IR channel beam profile was measured using a pyroelectric array detector (Spiricon, Pyrocam III-HR). Fig. 20 (c-d) shows the focused, near-field beam profiles after focusing with a spherical mirror ($f = 500$ mm). As the resolution of the pyroelectric array detector is insufficient to resolve the focused IR beam dimensions, the Si-based detector measured the corresponding two-photon absorption signal (see Fig. 20 (d)). Because this nonlinear process scales quadratically with the intensity of the IR beam, the measured beam size must be multiplied by $\sqrt{2}$. The results were cross-checked by knife-edge measurements, which differed only by $<$ 2%. The resulting beam diameters at focus were measured to be ~ 120 and ~ 112 μm for the NIR and IR channels, respectively, with a longitudinal focus position displacement of ≈ 100 μm. To check whether the beams overlap in space and time at 1 kHz repetition rate, hence for every single shot, we built a characterization station that evaluates the spatiotemporal overlap of both beams of each channel in the near-field (see Fig. 21 (a)). From a weak replica of the combined beam, the IR beam is frequency-doubled in a 100 μm-thick Type-I BBO-crystal (see Fig. 21 (b)) and is spatially-interfered with the NIR beam. A band-pass filter enhances the fringe contrast. After that, a wire grid polarizer is placed just before a high-speed camera (Basler, acA640-750um) to equalize the contribution of NIR and IR-SHG. By operating in this every-single-shot mode, the spatial interference does not average out, and its evolution can be directly linked to the CEP and RP variations. Figure 21 (c-d) shows the corresponding near-field spatial interference when the beams overlap spatially, with the RP set for (c) destructive interference and (d) constructive interference. This characterization is performed in parallel to an ongoing experiment, allowing continuous online monitoring of the spatio-temporal overlap. For the long-term stabilization of

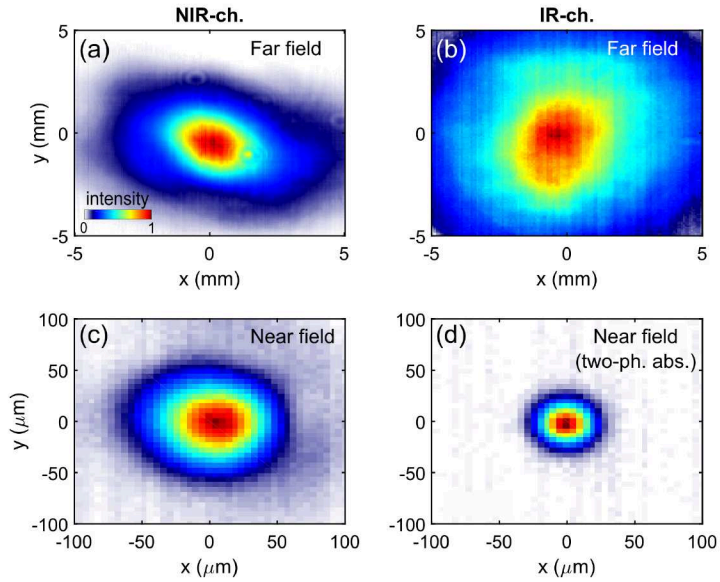

Fig. 20. NIR and IR channel far- and near-field beam profiles. Far-field beam profiles of **(a)** NIR and **(b)** IR channels and their respective near field **(c-d)** after a spherical mirror (f = 500 mm). A Si-based detector was used for (a), (c-d) and a pyroelectric array detector for (b). **(d)** shows the two-photon absorption signal resulting from the focused IR channel.

the beam pointing, an active stabilization system (TEM, Aligna) is employed for each constituent beam. After beam combination, a reflection from a thin glass plate derives a weak replica of the synthesized beam, which is then re-split into NIR and IR beams by dichroic mirrors and fed to the position-sensitive detectors (PSDs). The IR beam is additionally frequency-doubled in front of the PSD to match the spectral sensitivity of the Si-based detector.

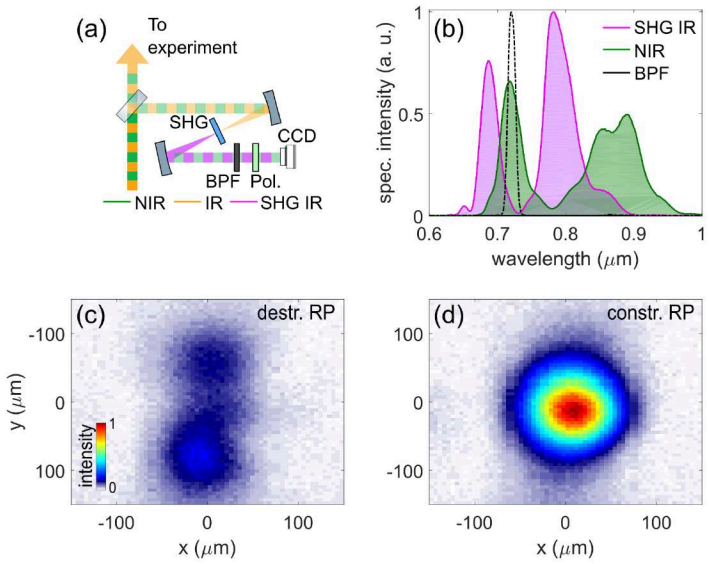

Fig. 21. Spatiotemporal overlap of NIR and IR beams. **(a)** Experimental setup. A pick-up deviates a portion of the beam towards the beam analysis setup. Second harmonic generation (SHG) of the IR beam is produced to beat with the NIR beam. A band-pass filter (BPF) ensures a visible fringe contrast, and a polarizer (Pol.) allows to equalize the contribution of NIR and SHG of IR beams. A charge-coupled device (CCD) detector records the resulting spatial interference. **(b)** Corresponding spectra. Spatiotemporal superposition between both beams at different RP values showing destructive **(c)** and constructive **(d)** interference.

7. Waveform reproducibility characterized by attosecond streaking

The measurement of the precise synthesized waveform is quite challenging for most pulse characterization methods, mainly due to the wide bandwidth. Apart from the temporal pulse characterization via two-dimensional spectral shearing interferometry, attosecond streaking was employed to directly map the vector potential of the electric field in an oscilloscope-like trace. In this technique, the generated isolated attosecond extreme ultraviolet/soft X-ray pulse ionizes a gas, and a superimposed optical field, in this case a replica of the synthesized pulse, modulates the kinetic energy of the liberated electrons. As a result of the single-step photoionization, the photoelectron spectrum closely resembles the spectrum of the attosecond pulse, lowered by the ionization potential of the gas. The replica of the optical, synthesized field, whose polarization is oriented parallel to the drift tube of the time-of-flight electron spectrometer, streaks the electron energies. The modulation of the electron energy depends on the delay between the ionization time (by the attosecond pulse) and the optical field. By sequentially recording photoelectron spectra at different delays between the isolated attosecond pulse (IAP) and the optical field, it is possible to access both the vector potential of the optical waveform and (by retrieval/reconstruction algorithms) also the spectral phase of the attosecond pulse. Due to the time-consuming delay scan and the highly nonlinear processes involved, the attosecond streaking technique is among the most demanding pulse characterization measurements in terms of the required shot-to-shot stability of the pulses involved, representing the ultimate benchmark for the PWS. The waveform must be highly repeatable to generate identical isolated attosecond pulses in the high-harmonics gas source. In Fig. 22a, we show the spectral intensity stability of different isolated attosecond pulses generated by the PWS. We observed a stability of 7% rms at 40 eV when averaged over 50

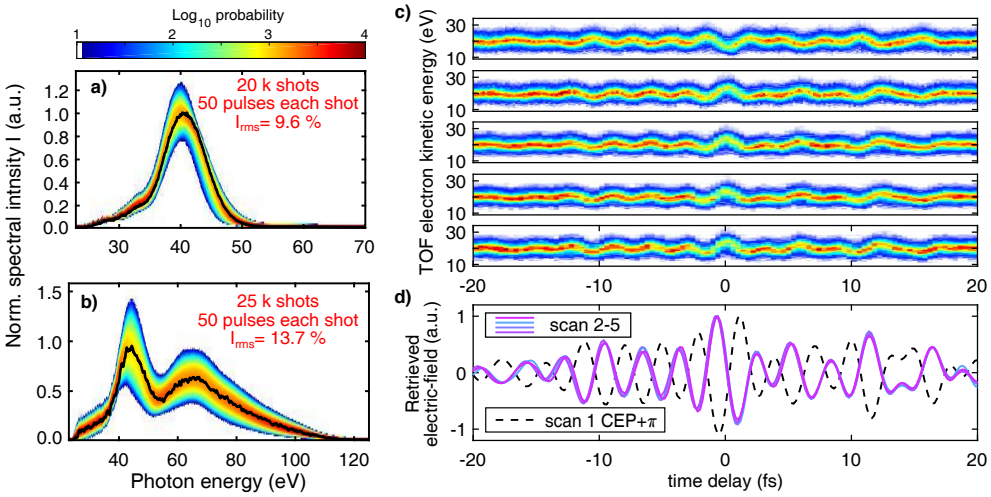

Fig. 22. **(a, b)** Spectral stability of isolated attosecond pulses generated via HHG with two different pulse synthesis settings as logarithmic color heat map and the mean spectrum over 20, and 25k shots each (black). The intensity of the generated attosecond pulses reach a high stability with a remaining rms fluctuation between 10-14%. **(c)** Top: Two finely sampled attosecond streaking traces with 180° CEP shift. Bottom three repeated streaking traces with the same CEP-setting demonstrating repeatability. **(d)** Retrieved electric-fields from **(c)** by a center of mass algorithm [46].

shots. Multiple consecutive attosecond streaking traces were recorded with identical waveforms over 2 hours (4 successive traces) in order to evaluate the long-term waveform stability (see Fig. 22b). A center-of-mass waveform retrieval algorithm yields retrieved electrical waveforms with excellent agreement and without significant drifts or waveform modifications (see Fig. 22c). Observed differences in the retrieved fields can be attributed to interferometric drifts between the isolated attosecond pulses and the streaking field, as the attosecond beamline was not actively stabilized. Additionally, to demonstrate control over the synthesized waveform, a π shift in the CEP was introduced in one streaked waveform [46].

8. Conclusions and perspectives

This paper presents the enabling techniques for parallel parametric waveform synthesis (PWS). With these technologies, the PWS can deliver stable and controllable non-sinusoidal optical waveforms with sub-cycle durations, mJ-level energy at 1 kHz repetition rate. Because this technology is based on OP(CP)A, it is intrinsically scalable to higher pulse energy and average power. We modeled the phase propagation in the different OP(CP)As of the PWS. The contribution of pump-seed temporal jitter in the narrowband OPA-seeder was quantified in a previous publication, and conditions to optimize the CEP stability were obtained. Here we extend the analytic description to the broadband OP(CP)As of the spectral channels, proving that small pump-seed relative arrival time fluctuations do not influence the signal CEP if large stretching ratios are used, and the pulses are fully recompressed at the interaction point. These considerations on the timing dynamics clear the way to energy and power scaling of the PWS since different laser technologies could be adapted.

So far, we developed a two-channel (NIR and IR) OPA-based PWS that delivers 1.7-octaves of bandwidth, durations down to about 0.6 cycles (full-width at half-maximum, FWHM), and energies up to $\sim$ 0.5 mJ. The system is ready to be upgraded with an additional channel covering

the visible spectral range.

Realizing PWS setups requires a careful choice of optical, mechanical, and active stabilization techniques. CEP-controlled seed drivers are derived from non-CEP-stabilized laser beams via difference-frequency generation in a two-stage OPA. Multi-octave wide, yet highly phase coherent, seed pulses are obtained by spectral broadening of CEP-controlled driver pulses in separate WLG-stages, each optimized for the phase-matching bandwidth of different ultrabroadband OPAs. The three-stage OPAs yield few-cycle pulses covering different spectral regions (VIS, NIR, IR) with energies of 0.1-0.5 mJ. The NIR and IR pulses are coherently combined to two octaves (or more) of synthesized bandwidth corresponding to sub-cycle pulses. An active timing stabilization system based on in-line multi-phase meters and single-shot phase retrieval allows for stabilization and control of repeatable pulses over hours of operation, allowing even for demanding experimental applications such as attosecond streaking and hence suitable for attosecond-resolved experiments. A reduced set of synthesis parameters allows accessing almost the complete manifold of possible waveforms while keeping the system complexity low enough to allow for reliable operation. A modular optical setup exhibiting superb timing stability and careful spatial overlap characterization allows for the reproducibility required by attosecond pump-probe spectroscopic applications. In the next step, a third spectral channel will be fully integrated to yield an additional pulse in the visible spanning 520-700 nm with 150 μJ of pulse energy and 6 fs in duration. This upgrade will allow for pulses to be as short as 1.9 fs in duration and with even more intricate non-sinusoidal waveform customization. Furthermore, additional degrees of freedom for waveform design arise. At this level, a genetic algorithm of adaptive waveform control might become necessary to help optimize the characteristics of the isolated attosecond pulses, as plain waveform scanning would take multiple days due to the additional degrees of freedom.

In the next stage of development, this approach for waveform synthesis will benefit from higher power pump lasers (e.g. Yb-based lasers). Since the pump power need to be distributed among multiple OPA stages, a multi-beam Ti:Sa laser amplifier could be used to increase the pulse energy or repetition rate of the current PWS implementation.

Sub-cycle tailored waveforms capable of driving tunable isolated attosecond pulse generation over a broad energy range (up to the soft x-ray) will open up new possibilities for attosecond pump-probe experiments. This includes schemes where by utilizing sub-cycle waveforms to drive strong-field ionization will be possible to confine the pump-excitation to a few hundreds of attoseconds, enabling as-pump/as-probe resolution.

Acknowledgement

G. M. Rossi would like to thank Dr. Audrius Zaukevičius for fruitful discussions.

Funding

We gratefully acknowledge support from Deutsches Elektronen-Synchrotron (DESY) of the Helmholtz Association, from the Cluster of Excellence 'CUI: Advanced Imaging of Matter' of the Deutsche Forschungsgemeinschaft (DFG)—EXC 2056—project ID 390715994, the priority programme 'Quantum Dynamics in Tailored Intense Fields' (QUTIF) of the DFG (SPP1840 SOLSTICE) and H2020 European Research Council (ERC) (FP7/2007-2013, ERC 609920-AXSIS).

Disclosures

The authors declare no conflicts of interest.

Data availability

The data underlying the results presented in this paper are available from the authors upon reasonable request.

References

1. G. Cerullo, M. Nisoli, S. Stagira, and S. De Silvestri, "Sub-8-fs pulses from an ultrabroadband optical parametric amplifier in the visible." Opt. letters **23**, 1283–1285 (1998).
2. G. Cerullo and S. De Silvestri, "Ultrafast optical parametric amplifiers," Rev. Sci. Instruments **74**, 1–18 (2003).
3. D. Brida, C. Manzoni, G. Cirmi, M. Marangoni, S. Bonora, P. Villoresi, S. De Silvestri, and G. Cerullo, "Few-optical-cycle pulses tunable from the visible to the mid-infrared by optical parametric amplifiers," J. Opt. A: Pure Appl. Opt. **12** (2010).
4. M. Nisoli, S. De Silvestri, and O. Svelto, "Generation of high energy 10 fs pulses by a new pulse compression technique," Appl. Phys. Lett. **68**, 2793–2795 (1996).
5. C.-H. Lu, Y.-J. Tsou, H.-Y. Chen, B.-H. Chen, Y.-C. Cheng, S.-D. Yang, M.-C. Chen, C.-C. Hsu, and A. H. Kung, "Generation of intense supercontinuum in condensed media," Optica **1**, 400 (2014).
6. J. Schulte, T. Sartorius, J. Weitenberg, A. Vernaleken, and P. Russbueldt, "Nonlinear pulse compression in a multi-pass cell," Opt. Lett. **41**, 4511 (2016).
7. G. M. Rossi, R. E. Mainz, Y. Yang, F. Sheiba, M. A. Silva-Toledo, S.-H. Chia, P. D. Keathley, S. Fang, O. D. Muecke, C. Manzoni, G. Cerullo, G. Cirmi, and F. X. Kärtner, "Sub-cycle millijoule-level parametric waveform synthesizer for attosecond science," Nat. Photonics **14**, 629–635 (2020).
8. Y. Yang, R. E. Mainz, G. M. Rossi, F. Scheiba, M. A. Silva-Toledo, P. D. Keathly, G. Cirmi, and F. X. Kärtner, "Strong-field coherent control of isolated attosecond pulse generation," Nat. Commun. **12**, 6641 (2021).
9. P. A. Andrekson, H. Sunnerud, S. Oda, T. Nishitani, and J. Yang, "Ultrafast, atto-Joule switch using fiber-optic parametric amplifier operated in saturation," Opt. Express **16**, 16956 (2008).
10. O. V. Chekhlov, J. L. Collier, I. N. Ross, P. K. Bates, M. Notley, C. Hernandez-Gomez, W. Shaikh, C. N. Danson, D. Neely, P. Matousek, S. Hancock, and L. Cardoso, "35 J broadband femtosecond optical parametric chirped pulse amplification system," Opt. Lett. **31**, 3665 (2006).
11. H. Höppner, A. Hage, T. Tanikawa, M. Schulz, R. Riedel, U. Teubner, M. J. Prandolini, B. Faatz, and F. Tavella, "An optical parametric chirped-pulse amplifier for seeding high repetition rate free-electron lasers," New J. Phys. **17**, 053020 (2015).
12. A. Baltuška, T. Fuji, and T. Kobayashi, "Controlling the Carrier-Envelope Phase of Ultrashort Light Pulses with Optical Parametric Amplifiers," Phys. Rev. Lett. **88**, 133901 (2002).
13. G. M. Rossi, L. Wang, R. E. Mainz, H. Çankaya, F. X. Kärtner, and G. Cirmi, "CEP dependence of signal and idler upon pump-seed synchronization in optical parametric amplifiers," Opt. Lett. **43**, 178 (2018).
14. T. W. Hänsch, "A proposed sub-femtosecond pulse synthesizer using separate phase-locked laser oscillators," Opt. Commun. **80**, 71–75 (1990).
15. C. Manzoni, O. D. Mücke, G. Cirmi, S. Fang, J. Moses, S. W. Huang, K. H. Hong, G. Cerullo, and F. X. Kärtner, "Coherent pulse synthesis: Towards sub-cycle optical waveforms," Laser Photonics Rev. **9**, 129–171 (2015).
16. M. T. Hassan, A. Wirth, I. Grguraš, A. Moulet, T. T. Luu, J. Gagnon, V. Pervak, and E. Goulielmakis, "Attosecond photonics: Synthesis and control of light transients," Rev. Sci. Instruments **83**, 111301 (2012).
17. S.-W. Huang, G. Cirmi, J. Moses, K.-H. Hong, S. Bhardwaj, J. R. Birge, L.-J. Chen, E. Li, B. J. Eggleton, G. Cerullo, and F. X. Kärtner, "High-energy pulse synthesis with sub-cycle waveform control for strong-field physics," Nat. Photonics **5**, 475–479 (2011).
18. C. Manzoni, S.-W. Huang, G. Cirmi, P. Farinello, J. Moses, F. X. Kärtner, and G. Cerullo, "Coherent synthesis of ultra-broadband optical parametric amplifiers," Opt. Lett. **37**, 1880 (2012).
19. H. Liang, P. Krogen, Z. Wang, H. Park, T. Kroh, K. Zawilski, P. Schunemann, J. Moses, L. F. DiMauro, F. X. Kärtner, and K.-H. Hong, "High-energy mid-infrared sub-cycle pulse synthesis from a parametric amplifier," Nat. Commun. **8**, 141 (2017).
20. A. Kessel, V. E. Leshchenko, O. Jahn, M. Krüger, A. Münzer, A. Schwarz, V. Pervak, M. Trubetskov, S. A. Trushin, F. Krausz, Z. Major, and S. Karsch, "Relativistic few-cycle pulses with high contrast from picosecond-pumped OPCPA," Optica **5**, 434 (2018).
21. A. Alismail, H. Wang, G. Barbiero, N. Altwaijry, S. A. Hussain, V. Pervak, W. Schweinberger, A. M. Azzeer, F. Krausz, and H. Fattahi, "Multi-octave, CEP-stable source for high-energy field synthesis," Sci. Adv. **6**, 1–8 (2020).
22. B. Xue, Y. Tamaru, Y. Fu, H. Yuan, P. Lan, O. D. Mücke, A. Suda, K. Midorikawa, and E. J. Takahashi, "Fully stabilized multi-TW optical waveform synthesizer: Toward gigawatt isolated attosecond pulses," Sci. Adv. **6**, 2–11 (2020).
23. M. Bellini and T. W. Hänsch, "Phase-locked white-light continuum pulses: toward a universal optical frequency-comb synthesizer," Opt. Lett. **25**, 1049 (2000).
24. T. Nubbemeyer, M. Kaumanns, M. Ueffing, M. Gorjan, A. Alismail, H. Fattahi, J. Brons, O. Pronin, H. G. Barros, Z. Major, T. Metzger, D. Sutter, and F. Krausz, "1 kW, 200 mJ picosecond thin-disk laser system," Opt. Lett. **42**, 1381 (2017).
25. H. Stark, J. Buldt, M. Müller, A. Klenke, and J. Limpert, "1 kw, 10 mj, 120 fs coherently combined fiber cpa laser system," Opt. Lett. **46**, 969–972 (2021).
26. B. E. Schmidt, A. Hage, T. Mans, F. Légaré, and H. J. Wörner, "Highly stable, 54mj yb-innoslab laser platform at 0.5kw average power," Opt. Express **25**, 17549–17555 (2017).
27. Y. Liu, U. Demirbas, M. Kellert, J. Thesinga, H. Cankaya, Y. Hua, L. E. Zapata, M. Pergament, and F. X. Kärtner, "Eight-pass yb:ylf cryogenic amplifier generating 305-mj pulses," OSA Continuum **3**, 2722–2729 (2020).

28. U. Demirbas, M. Kellert, J. Thesinga, Y. Hua, S. Reuter, M. Pergament, and F. X. Kärtner, "Highly efficient cryogenic Yb:YLF regenerative amplifier with 250 W average power," Opt. Lett. **46**, 3865 (2021).
29. A. Baltuška, M. Uiberacker, E. Goulielmakis, R. Kienberger, V. S. Yakovlev, T. Udem, T. W. Hänsch, and F. Krausz, "Phase-Controlled Amplification of Few-Cycle Laser Pulses," IEEE J. on Sel. Top. Quantum Electron. **9**, 972–989 (2003).
30. R. Grigutis, G. Tamošauskas, V. Jukna, A. Risos, and A. Dubietis, "Supercontinuum generation and optical damage of sapphire and yag at high repetition rates," Opt. Lett. **45**, 4507–4510 (2020).
31. G. M. Rossi, "Parametric Waveform Synthesis," Ph.D. thesis, Universität Hamburg (2019).
32. S.-H. Chia, G. Cirmi, S. Fang, G. M. Rossi, O. D. Mücke, and F. X. Kärtner, "Two-octave-spanning dispersion-controlled precision optics for sub-optical-cycle waveform synthesizers," Optica **1**, 315–322 (2014).
33. O. Razskazovskaya, F. Krausz, and V. Pervak, "Multilayer coatings for femto- and attosecond technology," Optica **4**, 129–138 (2017).
34. V. Pervak, O. Razskazovskaya, I. B. Angelov, K. L. Vodopyanov, and M. Trubetskov, "Dispersive mirror technology for ultrafast lasers in the range 220–4500 nm," Adv. Opt. Technol. **3**, 55–63 (2014).
35. T. Popmintchev, M. C. Chen, D. Popmintchev, P. Arpin, S. Brown, S. Ališauskas, G. Andriukaitis, T. Balčiunas, O. D. Mücke, A. Pugzlys, A. Baltuška, B. Shim, S. E. Schrauth, A. Gaeta, C. Hernández-García, L. Plaja, A. Becker, A. Jaron-Becker, M. M. Murnane, and H. C. Kapteyn, "Bright coherent ultrahigh harmonics in the kev x-ray regime from mid-infrared femtosecond lasers," Science **336**, 1287–1291 (2012).
36. P. Baum, S. Lochbrunner, J. Piel, and E. Riedle, "Phase-coherent generation of tunable visible femtosecond pulses." Opt. letters **28**, 185–187 (2003).
37. R. E. Mainz, G. M. Rossi, G. Cirmi, Y. Yang, S.-h. Chia, E. J. Takahashi, O. D. Mücke, and F. X. Kärtner, "Can sub-optical-cycle parametric waveform synthesizers be seeded by separate bulk white-light supercontinua?" in *CLEO US 2016,* (2016), pp. 2–3.
38. R. E. Mainz, "Sub-Cycle Light Field Synthesizer for Attosecond Science," Ph.D. thesis, Universität Hamburg (2019).
39. R. E. Mainz, G. M. Rossi, Y. Yang, D. M. Oliver, G. Cirmi, and X. K. Franz, "Three-octave-wide phase-stable seeding scheme for parallel parametric waveform synthesizers," in *CLEO: Science and Innovations US 2018,* (2018), p. SF3N.5.
40. M. Görbe, K. Osvay, C. Grebing, and G. Steinmeyer, "Isochronic carrier-envelope phase-shift compensator," Opt. Lett. **33**, 2704 (2008).
41. C. Manzoni and G. Cerullo, "Design criteria for ultrafast optical parametric amplifiers," J. Opt. **18**, 103501 (2016).
42. D. J. Maas, D. I. Duncan, R. B. Vrijen, W. J. Van Der Zande, and L. D. Noordam, "Vibrational ladder climbing in NO by (sub)picosecond frequency-chirped infrared laser pulses," Chem. Phys. Lett. **290**, 75–80 (1998).
43. G. M. Rossi, R. E. Mainz, F. Scheiba, M. A. Silva-Toledo, G. Cirmi, and F. X. Kärtner, "Phase Stabilization in a Sub-Cycle Parametric Waveform Synthesizer," in *Ultrafast Optics XII 2019,* ((European Optical Society, 2019), 2019), p. P1.19.
44. T. R. Schibli, J. Kim, O. Kuzucu, J. T. Gopinath, S. N. Tandon, G. S. Petrich, L. A. Kolodziejski, J. G. Fujimoto, E. P. Ippen, and F. X. Kärtner, "Attosecond active synchronization of passively mode-locked lasers by balanced cross correlation," Opt. Lett. **28**, 947 (2003).
45. M. B. Gaarde, J. L. Tate, and K. J. Schafer, "Macroscopic aspects of attosecond pulse generation," J. Phys. B: At. Mol. Opt. Phys. **41**, 132001 (2008).
46. M. A. Silva-Toledo, G. M. Rossi, R. E. Mainz, Y. Yang, F. Scheiba, P. D. Keathley, G. Cirmi, and F. X. Kärtner, "Waveform reproducibility from an opa-based parallel synthesizer," in *OSA High-brightness Sources and Light-driven Interactions Congress 2020 (EUVXRAY, HILAS, MICS),* (Optica Publishing Group, 2020), p. HF1B.5.